




Observing EAGLE galaxies with *JWST*: predictions for Milky Way progenitors and their building blocks

Tilly A. Evans ^{1,2}★, Azadeh Fattahi ¹, Alis J. Deason ^{1,2} and Carlos S. Frenk¹

¹*Institute for Computational Cosmology, Department of Physics, Durham University, South Road, Durham DH1 3LE, UK*

²*Centre for Extragalactic Astronomy, Department of Physics, Durham University, South Road, Durham DH1 3LE, UK*

Accepted 2022 August 22. Received 2022 July 22; in original form 2022 April 4

ABSTRACT

We present predictions, derived from the EAGLE Λ CDM cosmological hydrodynamical simulations, for the abundance and properties of galaxies expected to be detected at high redshift by the *James Webb Space Telescope* (*JWST*). We consider the galaxy population as a whole and focus on the sub-population of progenitors of Milky Way (MW) analogues, defined to be galaxies with accretion histories similar to the MW's, that is, galaxies that underwent a merger resembling the Gaia-Enceladus-Sausage (GES) event and that contain an analogue of the Large Magellanic Cloud (LMC) satellite today. We derive the luminosity function of all EAGLE galaxies in *JWST*/NIRCam passbands, in the redshift range $z = 2 - 8$, taking into account dust obscuration and different exposure times. For an exposure time of $T = 10^5$ s, average MW progenitors are observable as far back as $z \sim 6$ in most bands, and this changes to $z \sim 5$ and $z \sim 4$ for the GES and LMC progenitors, respectively. The progenitors of GES and LMC analogues are, on average, ~ 2 and ~ 1 mag fainter than the MW progenitors at most redshifts. They lie, on average, within ~ 60 and 30 arcsec, respectively, of their future MW host at all times, and thus will appear within the field of view of *JWST*/NIRCam. We conclude that galaxies resembling the main progenitor of the MW and its major accreted components should be observable with *JWST* beyond redshift 2, providing a new and unique window in studying the formation history of our own galaxy.

Key words: methods: numerical – galaxy: evolution – galaxy: formation.

1 INTRODUCTION

The *James Webb Space Telescope* (*JWST*) was designed to search for faint galaxies at the highest redshifts. Its primary imager, the Near InfraRed Camera (*JWST*/NIRCam), will cover wavelengths in the range $0.6\text{--}5\ \mu\text{m}$ and is expected to observe some of the earliest stars and galaxies (Beichman et al. 2012). These observations may reveal the early stages of galaxy formation and provide an important test of the Λ cold dark matter (Λ CDM) model of the universe, which predicts that galaxies are assembled hierarchically starting from small, faint fragments that form at high redshift.

Theoretical predictions are vital for the interpretation of the upcoming observations. Cosmological hydrodynamical simulations and semi-analytic modelling are the tools commonly employed for making such predictions (e.g. Cowley et al. 2018; Tacchella et al. 2018; Yung et al. 2019; Vogelsberger et al. 2020). For example Cowley et al. (2018) and Yung et al. (2019) used semi-analytic modelling to predict galaxy luminosity functions for *JWST*/NIRCam passbands at various redshifts. Similarly, Vogelsberger et al. (2020) used the IllustrisTNG hydrodynamical simulations for the same purpose and provided tailored predictions for two *JWST* surveys: the *JWST* Advanced Deep Extragalactic Survey (JADES) and the Cosmic Evolution Early Release Science Survey. Hydrodynamical simulations like this have the advantage that they can resolve the spatial distribution of gas in galaxies, allowing the effects of dust to be calculated in post-processing. Several estimates already exist of the bright end of the luminosity function (e.g. Oesch et al. 2014;

Finkelstein et al. 2015; Bouwens et al. 2015, 2021); *JWST* will extend these measurements to much fainter magnitudes.

As the best-studied galaxy in the Universe, the Milky Way (MW) holds a special place in studies of galaxy formation and evolution. Recent advances, largely driven by data from the *Gaia* satellite (Gaia Collaboration 2018), have painted a much more detailed picture of its assembly history than we had even a few years ago. In particular, a major accretion event, in which a large dwarf galaxy merged into the main progenitor was recently discovered, the ‘Gaia-Enceladus’ (Helmi et al. 2018) or ‘Gaia Sausage’ (Belokurov et al. 2018; hereafter GES). Another large accretion event that has been known for a long time is that of the Large Magellanic Cloud (LMC), now known to be a very massive satellite, with about 10 per cent of the MW's mass (e.g. Penarrubia et al. 2016; Erkal et al. 2019). A massive accretion, such as the LMC, has been shown to be important when interpreting the satellite population of the MW and their orbital properties (Patel, Besla & Sohn 2017a; Patel, Besla & Mandel 2017b). There are several other suggested merger events present in the MW's history, these events tend to be either lower in stellar mass or at higher redshifts and are not very well characterized (e.g. Forbes 2020; Kruijssen et al. 2020; Naidu et al. 2020, 2021; Horta et al. 2021).

The GES was discovered in *Gaia* chemodynamical data for the inner Galactic halo by two groups.¹ This stellar component is thought to be the remnant of the merger of a relatively massive dwarf galaxy ($M_* \sim 10^8\text{--}10^9 M_\odot$), with the MW's progenitor about 8–11 Gyr ago,

¹There is some debate as to whether or not these are the same event (e.g. Elias et al. 2020; Evans 2020).

* E-mail: tilly.evans@durham.ac.uk

which formed the majority of the galactic inner halo and left a debris of stars on highly radial orbits (e.g. Amorisco 2017; Fattahi et al. 2019; Mackereth et al. 2019). As shown by Evans et al. (2020), if the GES and LMC are the only massive ($\gtrsim 5 \times 10^8 M_\odot$) accretion events, the MW’s accretion history would be unusually quiet for a galaxy of this mass in the Λ CDM model. The presence of the LMC is also exceptional: as first shown by Benson et al. (2002), only ~ 10 per cent of MW analogues in Λ CDM simulations have satellites as massive as the LMC (see also Busha et al. 2011; Boylan-Kolchin, Bullock & Kaplinghat 2011b; Liu et al. 2011; Tollerud et al. 2011).

In this work, we analyse MW analogues identified in the EAGLE cosmological hydrodynamics simulations (Crain et al. 2015; Schaye et al. 2015). Our goal is to make predictions for the properties of their progenitors that are, in principle, accessible to the *JWST*. We will consider the progenitors of average MW-like haloes (defined at $z = 0$), as well as those of MW-analogues constrained by their accretion history. Evans et al. (2020) found that these analogues have lower mass at early times compared to average MW-like haloes, selected at $z = 0$. We also investigate the properties of the progenitors of the LMC and GES analogues.

This paper is organized as follows. The simulations and details of our definitions of MW, LMC, and GES analogues are discussed in Section 2. Our calculation of galaxy luminosities in the *JWST*/NIRCam passbands and the dust model we adopt are described in Section 3, where we also present predictions for properties of the overall galaxy population, such as the luminosity function at various redshifts. Results for the MW, LMC, and GES progenitors are presented in Section 4. Our paper ends with a discussion of our main results and our conclusions in Section 5.

2 EAGLE SIMULATIONS

The EAGLE project consists of a set of cosmological hydrodynamical simulations that follow the formation and evolution of galaxies in large periodic cosmological volumes (Crain et al. 2015; Schaye et al. 2015). The simulations were run using a highly modified version of the smooth particle hydrodynamic Tree-PM code P-GADGET3, which is based on the publicly available GADGET2 code, (Springel 2005). A full description of the galaxy formation model is presented in Schaye et al. (2015). In short, it includes homogeneous ultraviolet (UV)-X-ray background radiation, metallicity-dependant star formation and cooling, stellar evolution and feedback, supermassive blackhole accretion, and active galactic nucleus (AGN) feedback. The EAGLE model has been shown to reproduce many key features of the observed galaxy population, such as the stellar mass function at $z = 0.1$ and realistic sizes down to $\sim 10^8 M_\odot$, and produce galaxies with realistic mass profiles and rotation curves (see Schaller et al. 2015). Also, properties of MW-like galaxies in EAGLE have been shown to reproduce key features of our Galaxy (e.g. Mackereth et al. 2019; Thob et al. 2019; Evans et al. 2020).

The Friends-of-Friends algorithm (Davis et al. 1985) was used, with a linking length of $0.2 \times$ the mean interparticle separation, to identify dark-matter haloes. The SUBFIND algorithm (Springel 2005) iteratively finds the substructure and subhaloes within the Friends-of-Friends groups. The adopted cosmological parameters are based on the Planck Collaboration (2014); $\Omega_m = 0.307$, $\Omega_\lambda = 0.693$, $\Omega_{bar} = 0.048$, $H_0 = 67.77 \text{ km s}^{-1} \text{ Mpc}^{-1}$, and $\sigma_8 = 0.8288$.

Unless otherwise stated, we use the fiducial EAGLE run that has a periodic cubic volume of $(100 \text{ Mpc})^3$ and was run with the ‘REFERENCE’ parameters (REF-L0100N1504 in the nomenclature of Schaye et al. 2015). The initial mass for gas and matter particles are $9.6 \times 10^6 M_\odot$ and $1.81 \times 10^6 M_\odot$, respectively. For convergence

checks at the low mass, we use an EAGLE run with $8 \times$ better mass resolution, but in a smaller volume, $(50 \text{ Mpc})^3$, which has been simulated with the ‘RECAL’ parameters (Recal-L0050N1504) run from the Exploring Neutral Gas in EAGLE (ENGINe) simulations (Sykes et al. in preparation).² This simulation has been run only up to $z = 2$. For simplicity, we refer to these runs as ‘EAGLE-Ref’ and ‘EAGLE-Recal’, hereafter.

The stellar mass (M_*) of galaxies adopted in this work is calculated by summing the masses of bound star particles within 30 kpc of the centre of galaxies. A 30 kpc radius is appropriate for MW-mass galaxies at redshift $z = 0$, since the majority of the stars are within this radius. At higher redshifts, where galaxies are smaller, this boundary will include all of the particles in the galaxy. Unless mentioned otherwise, we include galaxies with stellar mass above $10^7 M_\odot$, corresponding to $N \sim 5$ and 44 star particles in the EAGLE-Ref and EAGLE-Recal runs, respectively. The stellar masses of EAGLE-Ref galaxies have been shown to converge down to $N \sim 5$ particles in Sawala et al. (2016).

Several element abundances, including Iron and Hydrogen, are tracked self-consistently in the simulations for gas and star particles. We convert those mass fractions to $[\text{Fe}/\text{H}]$, assuming a solar abundance of $12 + \log_{10}(N_{\text{Fe}}/N_{\text{H}}) = 7.5$ from Asplund et al. (2009) to assign magnitudes to each star particle (described in more detail in Section 3).

2.1 Analogue definitions

In this work, we make use of many different galaxy ‘groups’ and thus provide clear definitions below. We define a MW-like galaxy as any galaxy in EAGLE-Ref with halo mass in the range $M_{200} = (0.7 - 2) \times 10^{12} M_\odot$ (see Callingham et al. 2019, and references therein). ‘LMC-like’ group includes satellites, located inside R_{200}^3 of any MW-like galaxy at $z = 0$, and have stellar masses in the range $M_* = (1 - 4) \times 10^9 M_\odot$. ‘GES-like’ galaxies are any galaxies that have a stellar mass of $M_* = (0.5 - 1) \times 10^9 M_\odot$ when they merge with a MW-like galaxy between redshift $z = 1$ and 2 (8–10 Gyr ago). Note that we do not place any constraints on having a Local Group environment, which could affect the formation epoch of our haloes (Santistevan et al. 2020).

Our ‘MW analogues’ are MW-like galaxies with additional constraints on their accretion history, following Evans et al. (2020):

- (i) one LMC-like satellite present at $z = 0$ with no other more massive satellites.
- (ii) one GES-like merger event with no more massive mergers within the same time frame.
- (iii) finally, we require that these systems have a ‘merger free zone’ when there is an absence of massive mergers ($M_* > 0.5 \times 10^9 M_\odot$) between redshifts $z = 0$ and $z = 2$.

The definition of LMC satellites and GES mergers are deliberately broad in the hope of having better statistics. Table 1 gives the number of galaxies in each of the groups used throughout this paper and their median stellar masses at redshifts $z = 0$ and $z = 2$. More specific properties of the MW analogue systems are presented in Evans et al. (2020).

²This simulation has the same resolution as L025N0752 run in Schaye et al. (2015). We do not use the latter due to the small size of the box and much fewer number of galaxies

³The spherical radius with mean enclosed density 200 times the critical density of the universe.

Table 1. The number of galaxies in each of the galaxy groups studied in this work and their median $z = 0$ and $z = 2$ stellar masses.

Group	Number	Median $M_{*, z=0}$ ($\times 10^9 M_{\odot}$)	Median $M_{*, z=2}$ ($\times 10^8 M_{\odot}$)
MW-like	1078	20.3	23.8
LMC-like	169	1.89	1.96
GES-like	234	–	6.40
MW-analogue	7	14.4	10.4
LMC-analogue	7	1.29	2.10
GES-analogue	7	–	4.79

3 GALAXY LUMINOSITIES AND COLOURS

In this section, we describe how we calculate the dust-free magnitudes of the simulated galaxies for *JWST*/NIRCam passbands, as well as the absolute rest-frame UV. We also describe the model adopted throughout this work to account for dust attenuation.

3.1 Dust-free magnitudes

We use the initial mass function (IMF), age, and metallicity of simulated star particles, combined with publicly available stellar libraries to retrieve their spectral energy distributions (SEDs). We use the Flexible Stellar Population Synthesis (FSPS) code (Conroy, Gunn & White 2009; Conroy & Gunn 2010) with the MESA Isochrones and Stellar Tracks (Paxton et al. 2011, 2013, 2015; Choi et al. 2016; Dotter 2016) and MILES stellar library (Sanchez-Blazquez et al. 2006). The IMF adopted in the simulations is Chabrier (Chabrier 2003) with an initial mass range of $0.1 - 100 M_{\odot}$. The stellar isochrones cover the following range of age and metallicity: $-2.5 \leq [\text{Fe}/\text{H}] \leq 0.5$ with 12 intervals, and $5 \leq \log(\text{age}/\text{yr}) \leq 10.3$ with 107 equally spaced points (these intervals were pre-determined by FSPS). We identify the isochrone with the nearest metallicity and age to the stellar particles. If any of the star particles lie outside the age-metallicity grid of isochrones, they are also assigned to the nearest isochrone.⁴

The magnitudes in various passbands are retrieved by applying the response of each filter to the SED, which is done automatically by FSPS. For galaxies at higher redshifts ($z > 0$), the SED is redshifted before applying the filter. The total magnitude of each galaxy is calculated by adding the flux of all bound star particles within $r < 30$ kpc.

3.2 Dust model

We compute the dust attenuation for each star particle in the simulated galaxies using a semi-empirical approach, following a modified version of ‘model B’ in Vogelsberger et al. (2020). The modification accounts for the fact that the gas component in the EAGLE simulation is represented by the smoothed particle hydrodynamics (SPH) technique, rather than Arepo’s Voronoi mesh cells in IllustrisTNG. We smooth the gas particles over a cubic grid, as detailed below. There are two different components to the dust model: resolved dust from the interstellar medium (ISM) and unresolved dust from stellar birth clouds.

⁴We have checked that only a small fraction (3 percent) of star particles fall outside this grid at $z = 4$. Hence they would have negligible effect on the overall luminosity of each galaxy.

3.2.1 Resolved dust

The resolved dust attenuation is caused by cold ($< 10^4$ K) or star-forming gas in the ISM along the line of sight. Unless otherwise stated, the line-of-sight direction for each galaxy is random. We use the smoothing lengths of gas particles to smooth the density using the original EAGLE kernel, over a cubic grid with 1 kpc spacing. We then carry out the following calculations (for more detailed information see Vogelsberger et al. 2020, Section 3.2.2) to obtain the attenuation for each star particle,

$$\tau_V^{\text{res}} = \tau_{\text{dust}}(z) \left(\frac{Z_g}{Z_{\odot}} \right)^{\gamma} \left(\frac{N_H}{N_{H,0}} \right) \quad (1)$$

where N_H is the hydrogen column density along the line of sight ‘in front’ of the star particle, $\tau_{\text{dust}}(z)$ is the redshift-dependent scale factor for the optical depth that scales as the average dust-to-metal ratio, $\gamma = 1$, and $N_{H,0} = 2.1 \times 10^{21} \text{ cm}^{-2}$. The V-band optical depth, τ_V , values are then converted into the V-band dust attenuation using the following relation

$$A_V^{\text{res}} = -2.5 \log \left(\frac{1 - e^{-\tau_V^{\text{res}}}}{\tau_V^{\text{res}}} \right). \quad (2)$$

Since the optical depth and dust attenuation are both specific to the V-band, they need to be converted to the optical depth and dust attenuation for the passbands we are interested in (*JWST*/NIRCam and absolute rest-frame UV). To convert from V-band attenuation to attenuation for a given wavelength, λ , we adopt the Calzetti et al. (2000) relation (modified by Kriek & Conroy 2013, to include the UV bump) for local starburst galaxies such that:

$$A^{\text{res}}(\lambda) = \frac{A_V^{\text{res}}}{4.05} [k'(\lambda) + D(\lambda)] \left(\frac{\lambda}{\lambda_V} \right)^{\delta} \quad (3)$$

where $k'(\lambda)$ is the normalized attenuation curve for A_V :

$$k'(\lambda) = 4.05 + 2.659 \begin{cases} \left(-1.875 + \frac{1.040}{\lambda} \right), & \text{for } 0.63 \mu\text{m} < \lambda < 2.20 \mu\text{m} \\ \left(-2.156 + \frac{1.509}{\lambda} - \frac{0.198}{\lambda^2} + \frac{0.011}{\lambda^3} \right), & \text{for } 0.12 \mu\text{m} < \lambda < 0.63 \mu\text{m} \end{cases} \quad (4)$$

and $D(\lambda)$ parametrizes the UV bump that is given by:

$$D(\lambda) = \frac{E_b(\lambda \Delta \lambda)^2}{(\lambda^2 - \lambda_0^2)^2 + (\lambda \Delta \lambda)^2} \quad (5)$$

where $\lambda_0 = 217.5$ nm and $\Delta \lambda = 35$ nm are the central wavelength and full-width half maximum of the UV bump, respectively (Seaton 1979; Noll et al. 2009). The shape of the attenuation curve is purely characterized by δ as shown by the relation between E_b and δ found by Kriek & Conroy (2013):

$$E_b = (0.85 \pm 0.09) - (1.9 \pm 0.4)\delta \quad (6)$$

we assume $\delta = 0$ in order to apply no correction to the attenuation curve other than the addition of the UV bump as in Vogelsberger et al. (2020). The overall correction for the magnitude for the resolved dust component, in any given filter, is therefore:

$$M^{\text{dust}} = M^{\text{dust-free}} + A^{\text{res}}(\lambda). \quad (7)$$

3.2.2 Unresolved dust

The unresolved dust component of the model accounts for the stellar birth clouds around young stars that are not resolved in EAGLE. We

include this component by assuming that all star particles in a given galaxy will have the same dust attenuation from their birth clouds.⁵ The birth cloud V-band optical depth is given by:

$$\tau_V^{\text{unres}} = \begin{cases} 2\langle\tau_V^{\text{res}}\rangle, & \text{for } t' \leq t_{\text{disp}} \\ 0, & \text{for } t' > t_{\text{disp}} \end{cases} \quad (8)$$

where $\langle\tau_V^{\text{res}}\rangle$ is the average V-band optical depth of the whole galaxy [computed using equation (1)] and $t_{\text{disp}} = 10$ Myr is the dispersion time for the stellar birth cloud. Hence, if a star particle is younger than the dispersal time of the stellar birth cloud then all star particles satisfying this criteria will have the same additional optical depth value. Again, the optical depth needs to be converted to the attenuation, here we assume a simple uniform dust screen such that the solution for the radiative transfer equation takes the following form:

$$\begin{aligned} A_V^{\text{unres}} &= -2.5 \log \left(e^{-\tau_V^{\text{unres}}} \right) \\ &= 1.086 \tau_V^{\text{unres}}. \end{aligned} \quad (9)$$

The dust attenuation at other wavelengths is estimated using a simple power-law relation from Charlot & Fall (2000) for unresolved dust:

$$A^{\text{unres}}(\lambda) = A_V^{\text{unres}} \left(\frac{\lambda}{\lambda_V} \right)^{-0.7}. \quad (10)$$

Combining the resolved and unresolved dust then gives the total magnitude correction, in any filter, such that:

$$M^{\text{dust}} = M^{\text{dust-free}} + A^{\text{res}}(\lambda) + A^{\text{unres}}(\lambda). \quad (11)$$

We show the high redshift M_{UV} –stellar mass relation of simulated galaxies from the EAGLE-Ref run in the left column of Fig. 1 after applying dust attenuation, and compare them with the results of Vogelsberger et al. (2020) from IllustrisTNG, as well as observations from Song et al. (2016). Song et al. (2016) analysed data from the *Hubble Space Telescope*, which included ~ 7000 galaxies selected using photometric redshifts in the range $z = 3.5$ – 8.5 ; further details may be found in Song et al. (2016, and references therein). Grey points are individual galaxies and the orange curve with error bars shows the median stellar mass and the [16th–84th] percentiles at fixed magnitude. We only show results for redshifts $z = 4, 6,$ and 8 , for which data from Song et al. (2016) are available. Our results are in excellent agreement with those of Vogelsberger et al. (2020, model ‘C’), which is a more comprehensive and computationally expensive dust model using the radiative transfer method SKIRT (Baes et al. 2011; Camps, Baes & Saftly 2013; Saftly, Baes & Camps 2014; Camps & Baes 2015). Our dust model uses additional information from the particles in the simulation (unlike simple empirical models) and shows quantitatively similar results to the full radiative dust model (SKIRT). This is very reassuring that they show such excellent agreement. EAGLE galaxies are also consistent with observational data within the scatter. The right column of Fig. 1 shows the dust attenuation as a function of M_{UV} for redshifts $z = 4, 6,$ and 8 , indicating that our dust attenuation increases by approximately ~ 1 mag as M_{UV} magnitude changes from -18 to -22 , this result is consistent with Yung et al. (2019). This is due to brighter (more massive) galaxies having a larger amount of (cold) gas. We also compared our dust-corrected magnitudes with those of Trayford et al. (2015) who calculated the dust-free and dust-corrected SDSS apparent magnitudes for EAGLE-Ref galaxies using SKIRT

⁵Since we are only interested in the dust attenuation for galaxies as a whole, dust attenuation values for individual star particles are not as important.

at $z = 0.1$. Our results are consistent with theirs in the mass range $M_* > 1 \times 10^9 M_\odot$.

3.3 Luminosity functions

Luminosity functions give the comoving number density of galaxies at a given luminosity; they are typically represented by a Schechter function (Schechter 1976) with the following form in magnitude space,

$$\phi(m) = \frac{0.4 \ln(10) \phi^*}{10^{0.4(m-m^*)(\alpha^*+1)}} \exp \left(-10^{-0.4(m-m^*)} \right), \quad (12)$$

where ϕ^* is the normalization, M^* is the transition magnitude, and α^* is the faint-end slope parameter.

Fig. 2 shows the comoving luminosity function of the simulated galaxies before and after dust correction, and the corresponding Schechter fits in the *JWST* F200W passband. The best-fitting parameters for the Schechter function were calculated using a χ^2 method for magnitudes brighter than 30, with Poisson uncertainties (the best-fitting parameters for the *JWST* F200W passband are presented in Table 2).

Fig. 2 shows that including dust affects the bright end of the luminosity function more than the faint end. This is expected according to the right column of Fig. 1. Moreover, Fig. 2 shows that the dust has a larger impact at lower redshifts. This is expected since the average metallicity of galaxies is higher at lower redshifts due to past star formation.

Fig. 3 shows the dust-corrected luminosity function of the EAGLE galaxies at two resolution levels, alongside the results of IllustrisTNG (Vogelsberger et al. 2020). The solid line corresponds to a Schechter fit to galaxies in the EAGLE-Ref simulation (repeated from Fig. 2); points show the higher resolution results from EAGLE-Recal. Small differences between the luminosity functions, EAGLE-Ref and EAGLE-Recal, are expected, as the two models have slightly different parameters (see Schaye et al. 2015, for comparison of stellar mass functions at $z = 0$). Our results, however, indicate that the low-mass end slope of our Schechter fit is not significantly affected by the lower resolution of the EAGLE-Ref run for redshifts $z < 4$. At higher redshifts, $z = 6$ and 8 , the differences between EAGLE-Ref and EAGLE-Recal become larger but these differences are still consistent within Poisson uncertainties (see e.g. Fig. 4). The increasing difference between EAGLE-Ref and EAGLE-Recal is due to the slight differences in the parameters of subgrid models (see Schaye et al. 2015, for more information).

The dashed lines in Fig. 3 show the outcome of model C, a full radiative transfer dust approximation using SKIRT presented by Vogelsberger et al. (2020). Despite the good agreement of the $M_* - M_{UV}$ relation between our results and those of Vogelsberger et al. (2020), especially at $z < 5$, shown in Fig. 1, there are notable differences in the luminosity functions. This implies that the difference is mainly coming from the differences in the stellar mass functions, or equivalently stellar mass–halo mass relations, between the two sets of simulations. The largest difference is seen at the brighter end and at lower redshift, so it is likely due to the differences in AGN models and feedback. We note that Vogelsberger et al. (2020) used a combination of IllustrisTNG volumes; the largest one (TNG-300) is $\approx 30\times$ larger than the EAGLE-Ref volume and therefore better samples the bright end of the luminosity function. We show bins with fewer than 10 galaxies as faint points in Fig. 2. The crosses in Fig. 3 show the luminosity functions derived from JADES Extragalactic Ultra-deep Artificial Realization (JAGUAR; Williams et al. 2018). The foundations of the JAGUAR mock catalogue were

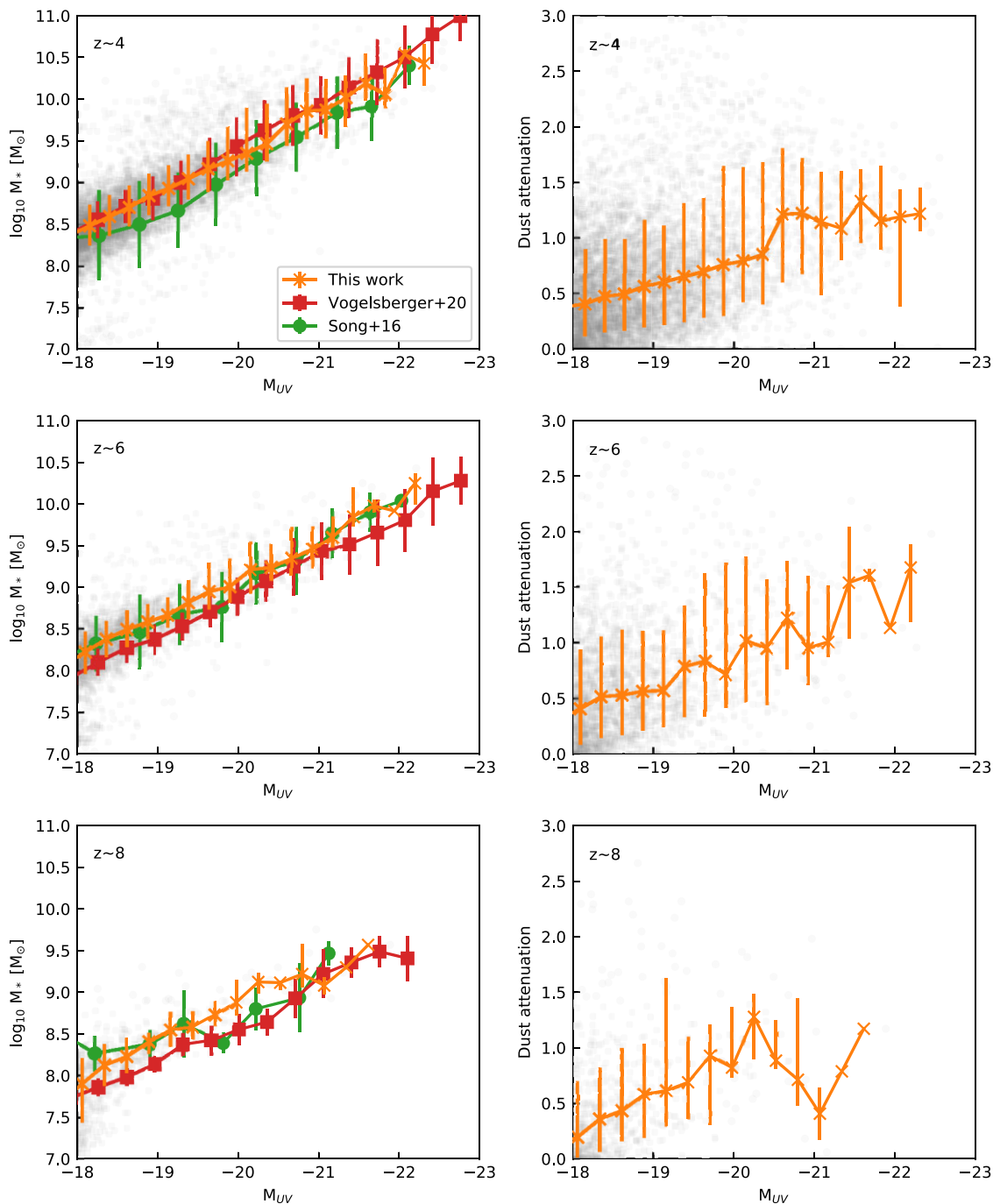


Figure 1. *Left column:* stellar mass versus dust-corrected rest-frame UV magnitude at redshifts $z = 4, 6,$ and 8 , with grey scatter points corresponding to individual galaxies from EAGLE-Ref and the orange line showing median and $[16^{\text{th}}-84^{\text{th}}]$ percentile at a fixed M_{UV} . The green connected circles and red connected squares show the results from the full radiative dust model in Vogelsberger et al. (2020), and observations from Song et al. (2016), respectively. *Right column:* dust attenuation as a function of magnitude at redshifts $z = 4, 6,$ and 8 for galaxies in EAGLE-Ref. Our analytic dust model produces comparable results to SKIRT and observations.

constructed using observations from Tomczak et al. (2014) and extrapolated to match the UV luminosity functions in Oesch et al. (2013), Bouwens et al. (2015, 2016), Calvi et al. (2016), Stefanon et al. (2017), and Oesch et al. (2018). The luminosity functions from JAGUAR agree well with our results, however, the luminosity functions are flatter throughout. Thus, the EAGLE simulations might underestimate the number of bright galaxies and overestimate the

number of faint galaxies that could be observed with *JWST*/NIRCam. The flattening of the faint end slope in the Williams et al. (2018) data is more pronounced at higher redshifts. This could be a result of the increasing difference in α^* values in the Schechter functions. Our α^* is consistent with Bouwens et al. (2015) at $z = 4$ who estimate the slope for the UV luminosity function to be -1.67 ± 0.05 ; however, at redshift $z \sim 8$, their slope is at least $\Delta\alpha^* \sim 0.9$ flatter.

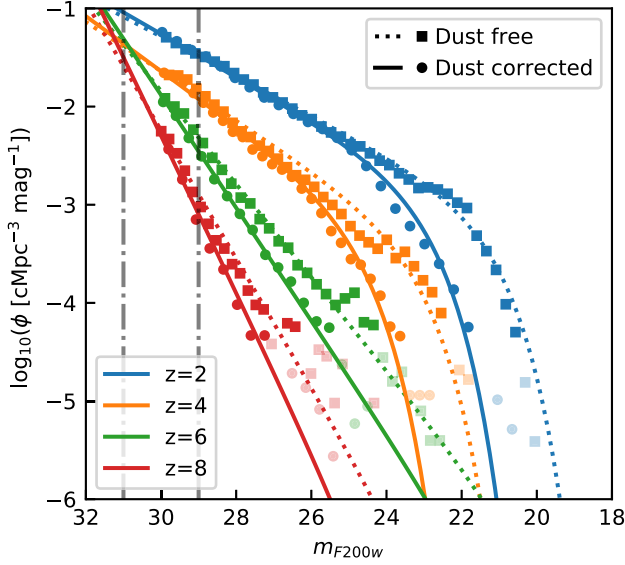


Figure 2. Luminosity functions of galaxies in the EAGLE-Ref simulation at different redshifts in the *JWST*/NIRCam F200W passband. The dust-free and dust-corrected luminosity functions are shown as square and circular points, respectively, with their corresponding Schechter fits as dotted and solid lines. Different redshifts are highlighted with different colours, as shown in the legend. Open faded symbols at the brighter end highlight bins with fewer than 10 galaxies per bin. The vertical dashed-dotted lines at limiting magnitudes of $m_{\text{lim}} = 29$ and 31 mag correspond to the faintest magnitudes that are observable with exposure times of $T_{\text{exp}} = 10^4$ s and 10^5 s, respectively.

Table 2. The best-fitting Schechter parameters for the *JWST* F200W passband at redshifts $z = 2, 4, 6,$ and 8 .

Redshift	ϕ^* ($\text{cMpc}^{-3} \text{mag}^{-1}$)	m^* (mag)	α^*
2	0.0018	23.09	-1.55
4	0.00091	24.83	-1.70
6	1×10^{-7}	21.03	-2.44
8	1×10^{-7}	24.06	-2.99

3.4 Number of galaxies in *JWST*/NIRCam field of view

Our predictions for the luminosity function of galaxies can be used to estimate the number of galaxies observable within a *JWST*/NIRCam field of view (FoV). We need to integrate the Schechter fits, as in equation (13), above the observable magnitude limit:

$$\begin{aligned} \phi_{\text{cum}}(< m_{\text{lim}}) &= \int_{L_{\text{lim}}}^{\infty} \phi(L) dL \\ &= \phi^* \Gamma_{\text{inc}}(\alpha^* + 1, 10^{-0.4(m_{\text{lim}} - m^*)}), \end{aligned} \quad (13)$$

where α^* , ϕ^* , and m^* are the parameters of the Schechter function, and $\Gamma_{\text{inc}}(a, z) = \int_z^{\infty} t^{a-1} e^{-t} dt$ is the upper incomplete gamma function; m_{lim} represents the magnitude limit that depends on the exposure time and signal-to-noise ratio (*SNR*). The limiting magnitudes used correspond to exposure times of $T = 10^4$ s and $T = 10^5$ s, with *SNR* = 10 and 5, respectively; these result in $m_{\text{lim}} = 29, 31$. $m_{\text{lim}} \sim 29$ corresponds to the expected limiting magnitude for the JADES-M survey.

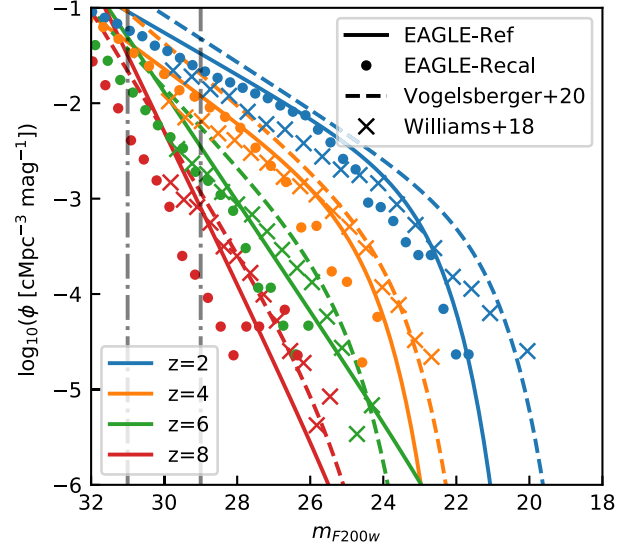


Figure 3. Dust-corrected luminosity functions for the *JWST*/NIRCam F200W passband for redshifts $z = 2, 4, 6,$ and 8 . Solid lines correspond to the Schechter fits for EAGLE-Ref luminosity functions (same as Fig. 2), whereas circles of the same colour show the higher resolution EAGLE-Recal luminosity functions. For comparison, the dashed lines represent the luminosity functions from the Illustris-TNG simulations, computed using radiative transfer dust model and presented in Vogelsberger et al. (2020). Crosses show the luminosity functions derived from the JAGUAR mock catalogue for *JWST* (Williams et al. 2018). The vertical dashed-dotted lines are the same as in Fig. 2.

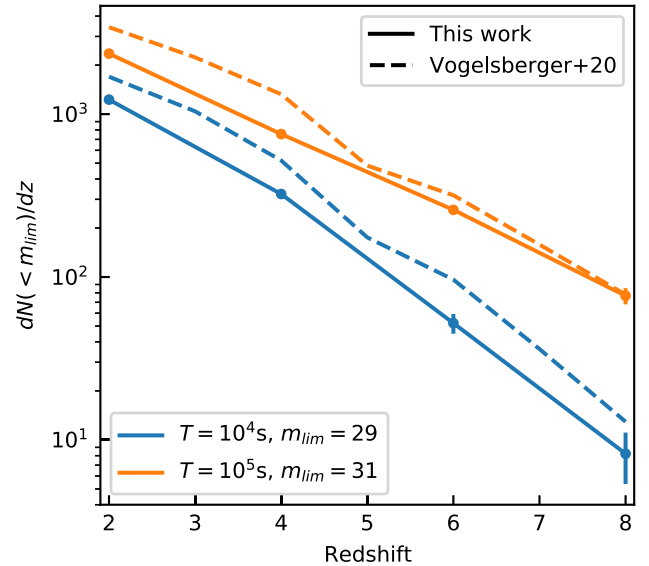


Figure 4. The expected number of galaxies as a function of redshift, in a *JWST*/NIRCam FoV (2.2×2.2 arcmin) that are above the detection limit with exposure times of $T = 10^4$ s and $T = 10^5$ s, and *SNR* = 10 and 5, respectively. These exposure times translate to limiting magnitude of $m_{\text{lim}} = 29$ and 31 , respectively. The solid and dashed lines correspond to our EAGLE-Ref results, and those of Vogelsberger et al. (2020), respectively. Error bars show the Poisson error on each value.

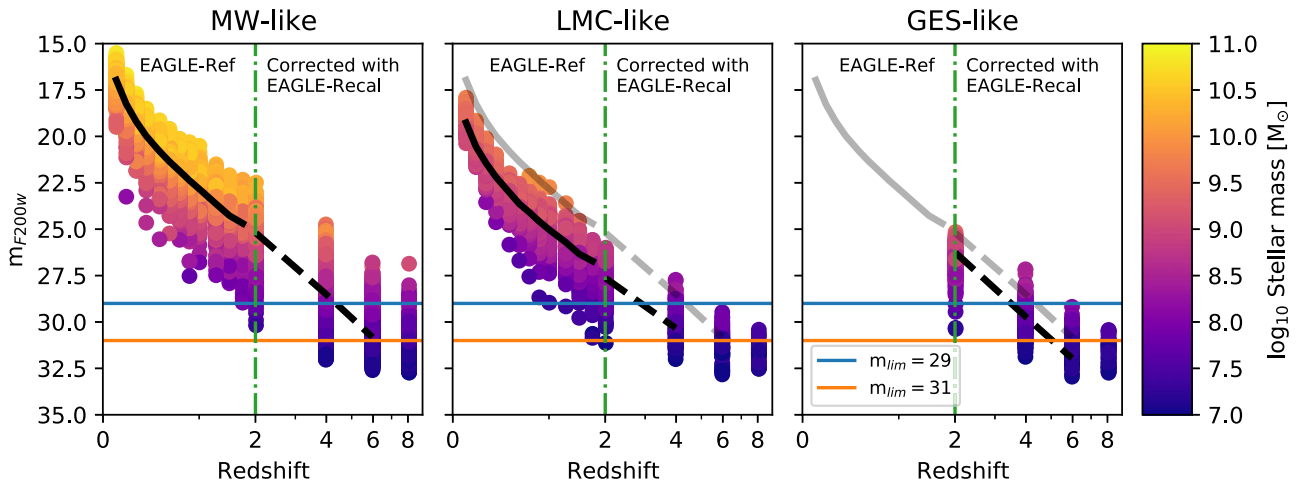


Figure 5. The apparent magnitude in the F200W passband as a function of redshift for progenitors of MW-like galaxies (*left*), the LMC-like satellites (*middle*), and GES-like galaxies (*right*) selected from the EAGLE-ref simulations. The points in each panel are coloured by the stellar mass, in logarithmic scale, of the galaxies as shown in the colour bar. Points to the left of the vertical dash-dotted line ($z = 2$) are magnitudes computed directly from EAGLE-Ref outputs, whereas magnitudes to the right of the line have been corrected using the $M_* - m_{F200W}$ relation of the higher resolution EAGLE-Recal simulation (see Appendix A for details). The solid black lines in each panel show the median apparent magnitude at each redshift up until the boundary at $z = 2$, beyond which it turns into dashed, indicating the transition to corrected magnitudes. The median line for the MW-like galaxies is repeated, as grey, in the middle and right-hand panel for reference. The two horizontal lines in blue and orange show the magnitude limits for exposure times of 10^4 s and 10^5 s, respectively with an $SNR = 10$ and 5, respectively.

Finally, the following relation can be used to compute the expected number of galaxies per unit redshift in the *JWST*/NIRCam FoV:

$$\frac{dN_{\text{exp}}}{dz} = \phi_{\text{cum}}(< m_{\text{lim}}) \frac{dV_{\text{com}}}{d\Omega dz}(z) \Delta\Omega, \quad (14)$$

where $dV_{\text{com}}/d\Omega dz$ is the differential comoving volume element described in equation (15) and $\Delta\Omega$ is the solid angle produced by the *JWST*/NIRCam FoV (2.2×2.2 arcmin).

$$\frac{dV_{\text{com}}}{d\Omega dz}(z) = \frac{c(1+z)^2 d_A(z)^2}{H_0 E(z)} \quad (15)$$

where d_A is the angular diameter distance and $H(z) = H_0 E(z)$ is the Hubble parameter at redshift z .

Fig. 4 shows our predictions for the observable number of galaxies per unit redshift in the *JWST*/NIRCam FoV for magnitude limits of $m_{\text{lim}} = 29$ and 31 (corresponding to the detection limits for exposure times of $T = 10^4$ s and $T = 10^5$ s, and $SNR = 10$ and 5, respectively). The error bars represent the Poisson error on each value.

Fig. 4 indicates that our expected number of galaxies is lower than those predicted in Vogelsberger et al. (2020) by roughly $N = 500(1000)$ at $z = 2$ for the $T = 10^4$ s ($T = 10^5$ s) exposure time. This is due to the systematically higher offset in the luminosity function of Vogelsberger et al. (2020) compared to EAGLE at all magnitudes at $z = 2$, as seen in Fig. 3. The same statement is true at redshift $z = 4$; however, this differs for the luminosity functions at redshifts $z = 6-8$ primarily between magnitudes 29 and 31 (vertical-dashed dotted lines), thus only affecting our expected number of galaxies for an exposure time of $T = 10^5$ s (shown in orange; corresponding to limiting magnitude of 31). Our expected number of galaxies for $T = 10^5$ s becomes much closer to the predictions of Vogelsberger et al. (2020) at high redshift that are only lower by $N \sim 60(1)$ at $z = 6$ ($z = 8$). We note that these differences are mainly driven by the faint end since the number of galaxies is dominated by galaxies in this regime. We also found that our predicted numbers of galaxies are consistent with Cowley et al. (2018), who used semi-analytic modelling techniques.

4 PROGENITORS OF MW, LMC, AND GES

In this section, we focus on progenitors of MW analogues that could be observed by *JWST*. All the magnitudes and colours shown in this section include dust attenuation. Our definition of MW-, LMC-, and GES-like galaxies, as well as MW analogues, are summarized in section 2.1.

Fig. 5 shows the evolution of dust-corrected F200W apparent magnitude as a function of redshift for the MW-like, LMC-like, and GES-like galaxies. Points are coloured according to their stellar mass as shown in the colour bar, and the lines show the median magnitudes at any given redshift. At lower redshifts $z < 2$, we show the magnitudes of progenitors, calculated directly from the EAGLE-Ref run. At $z > 2$, where stellar masses become smaller and resolution effects become important, we correct the magnitudes statistically using the stellar mass of the progenitors and the higher resolution EAGLE-Recal run. Details can be found in Appendix A. We apply the correction only at $z > 2$ and for progenitors with $M_* < 10^8 M_\odot$, which is where our calculated magnitudes show a large scatter at fixed stellar mass in the EAGLE-Ref run, due to the limited resolution of the simulation. The median lines turn from solid to dashed at $z > 2$ when magnitudes have been corrected, and the median line for the MW-like sample has been repeated in grey in the other two panels for reference.

As expected, the progenitors are typically fainter at earlier times, albeit with significant scatter, which increases towards higher redshift. This is particularly true for MW-like galaxies. For example, the median magnitude and the interquartile range for MW-like progenitors are $m_{F200W} = 20.8 \pm 0.58$ at $z \sim 0.5$ and they change to 25.2 ± 0.84 at $z \sim 2$.

At redshifts higher than $z \sim 3$, the fainter end of the magnitudes approach a constant value of $m_{F200W} \sim 33$ mag. This is not physical, and it is due to the low-mass progenitors not being identified by the halo-finder at early times. In these circumstances, we show the median assuming unidentified progenitors are all fainter than identified ones. We stop showing the median if more than 50 per cent of the progenitors in the sample are unidentified.

Table 3. The redshifts above which average progenitors of MW-, LMC-, and GES-like galaxies fall below the magnitude detection limit. Here, we assume exposure times of 10^4 s and 10^5 s, with an $SNR = 10$ and 5 , respectively, for each of the *JWST*/NIRCam photometric passbands.

	MW mass		LMC mass		GES mass	
	10^4 s	10^5 s	10^4 s	10^5 s	10^4 s	10^5 s
F070W	4.1	4.9	2.4	4.0	3.2	4.4
F090W	4.4	6.0	2.5	4.0	3.3	4.8
F115W	4.3	6.0	2.7	4.0	3.3	4.8
F150W	4.3	6.0	2.9	4.0	3.3	4.9
F200W	4.5	6.0	3.0	~ 4	3.5	5.0
F277W	4.5	6.0	3.0	~ 4	3.5	5.0
F356W	4.9	~ 6	3.4	~ 4	4.0	5.3
F444W	4.3	6.0	2.8	4.0	3.5	5.0

The two horizontal lines shown in Fig. 5 indicate the same detection limit of *JWST*/NIRCam used in the previous section: exposure times of $T = 10^4$ s and 10^5 s are shown as blue and orange, respectively. The median of MW-like progenitors is easily above the detection thresholds at $z < 4$. However, the large scatter causes the fainter progenitors to become undetectable from $z \sim 2$. LMC-like progenitors are on average fainter than the MW-like sample by only ~ 2 mag at most redshifts, and the two samples overlap significantly. The LMC-like sample is detectable on average to $z \sim 2.8$ for $T = 10^4$ s with almost none detectable beyond $z > 4$. The redshifts when the median magnitudes reach detection thresholds are summarized in Table 3, for various *JWST*/NIRCam passbands. The maximum redshifts observable for the three galaxy samples are all in the F356W passband, ~ 6 , ~ 4 , and 5.3 , respectively. The passband with the lowest maximum redshift for the three types of galaxies is the F070W passband. F356W is likely to be the most sensitive passband because it has the best transparency, whereas F070W is likely to be the worst because of the lower flux at the blue-end of the spectrum, as well as a lower transparency.

GES-like galaxies, by definition, merge with their host MW-like galaxy in the redshift range $z = 1 - 2$, and therefore no data are

shown at $z < 2$ for their progenitors in the right-hand panel of Fig. 5. Interestingly, the GES-like progenitor sample is only slightly fainter than the MW-like progenitors (~ 1.1 mag on average), and they are brighter than LMC progenitors. These results are shown in more detail for $z = 2$ in Fig. 6.

The first two panels of Fig. 6 show the magnitude (m_{F200W}) and stellar mass distributions of the MW-, LMC-, and GES-like progenitor samples at $z = 2$. We can see more clearly here that the progenitors of MW-like galaxies are, on average, brighter and more massive than progenitors of both LMC- and GES-like galaxies. In addition, GES-like galaxies are brighter than LMC-like galaxies with the medians differing by $\Delta(m) \sim 1.2$ and $\Delta(\log_{10}(M_*)) \sim 0.5$. The median magnitudes for progenitors of LMC-like galaxies at $z = 2$ are consistent with predictions made by Boylan-Kolchin et al. (2015) who estimate that the LMC would have had a dust-free absolute UV magnitude of $-15.6 \pm_{0.6}^{0.8}$. Our dust-free absolute M_{UV} for LMC-like galaxies at $z = 2$ is $M_{UV} \sim -15.7$. The distribution of masses and magnitudes for MW- and LMC-like progenitor galaxies have a greater spread than GES-like galaxies since the latter were constrained to have a mass between $M_* = 0.5 - 1 \times 10^9 M_\odot$ around redshift 2 before infall. The third panel of Fig. 6 shows the distribution of the stellar mass ratios between MW-like hosts and each of the LMC- and GES-like progenitor galaxies, all measured at $z = 2$. The ratio for GES-galaxies is higher than the ratio for LMC-galaxies by $\Delta(\log_{10}(M_*^i/M_*^{MW})) \sim 0.3$.

In all the panels of Fig. 6, the dashed vertical lines represent the median for the MW analogue galaxies, with individual galaxies shown as small arrows along the x -axis. The left two panels suggest that the progenitors of MW analogues are more similar in magnitude and stellar mass to the progenitors of GES-like galaxies than the MW-like sample as a whole. The right-hand panel shows that the mass ratios of LMC and GES components of the MW analogue progenitor systems are higher. This is due to the lower stellar mass of the MW analogue itself, which is lower than the average MW-like galaxy at higher redshift, as shown by Evans et al. (2020).

Not only is it important to know how far back in time the MW progenitors could be observed, but also to know *how likely* is it that

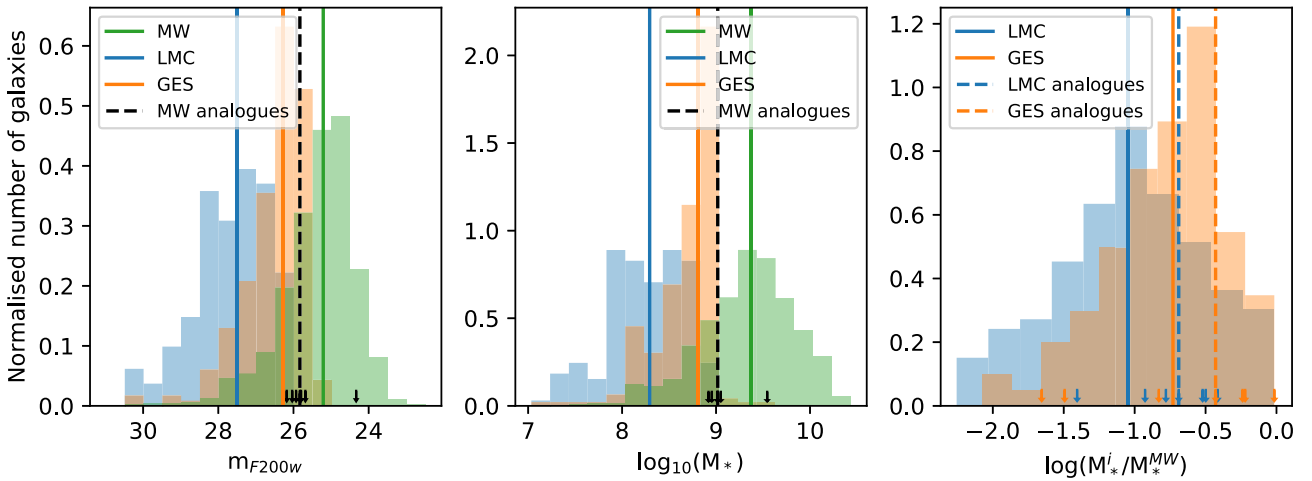


Figure 6. Comparison of the stellar masses and magnitudes of the progenitors of MW-, LMC-, and GES-like galaxies at $z = 2$. *Left:* magnitude distributions, in the F200W passband, for MW-, LMC-, and GES-like galaxies are shown as green, blue, and orange histograms, respectively. The medians of the distributions are marked with vertical solid lines of similar colour. The small black arrows along the x -axis show the magnitudes of the seven MW analogues (see text for details) and the vertical black-dashed line correspond to their median. *Middle:* same as the left but for stellar mass distributions. *Right:* the stellar mass ratios of the progenitors of LMC- and GES-like galaxies relative to their MW host, shown as blue and orange histograms, respectively. The solid lines of similar colour mark the median of the distributions. The small arrows along the x -axis and vertical-dashed lines correspond to the LMC- and GES-like objects associated to the seven MW analogues.

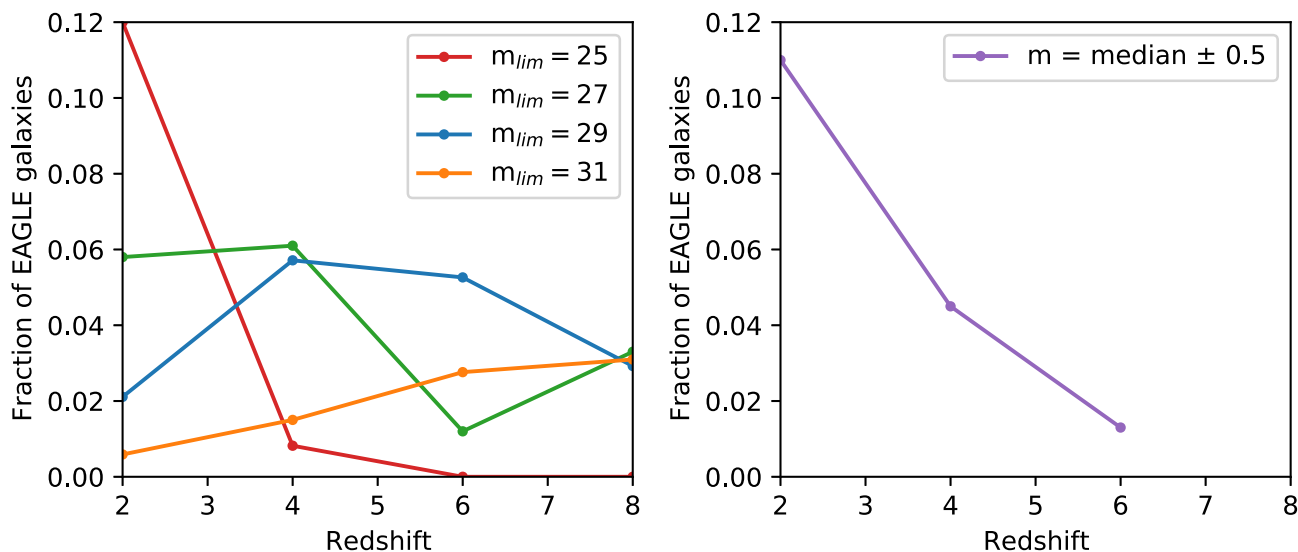


Figure 7. *Left:* the fraction of EAGLE-Ref galaxies above certain limiting magnitudes that are progenitors of MW-like galaxies, at different redshifts. The magnitude limits, in the F200W JWST/NIRCam passband, are shown in the legend: $m_{lim} = 25, 27, 29,$ and 31 corresponding to red, green, blue, and orange curves, respectively. *Right:* the fraction of galaxies in EAGLE-Ref that are progenitors of MW-like galaxies, and are observable and within a magnitude range, corresponding to ± 0.5 dex around the median apparent magnitude for F200W of Fig. 5, shown in purple.

they will be observed. The left-hand panel of Fig. 7 shows the fraction of observable ($m < m_{lim}$) EAGLE-Ref galaxies that are progenitors of MW-like galaxies, as a function of redshift. We consider four limiting magnitudes (m_{F200W}), $m_{lim} = 25, 27, 29,$ and 31 , shown in red, green, blue, and orange, respectively. At low redshifts, we find ~ 12 per cent of galaxies brighter than $m_{F200W} = 25$ to be progenitors of MW-like galaxies. However, this percentage drops to just ~ 1 per cent when including all galaxies above $m_{F200W} = 31$. At high redshift ($z > 6$), there are no longer any galaxies massive/bright enough to have a magnitude brighter than $m_{F200W} = 25$. At $z \sim 8$, the fainter limiting magnitudes ($m_{lim} = 27, 29,$ and 31) have the highest fraction of MW progenitors; ~ 4 per cent of galaxies are likely to be progenitors of MW-like galaxies.

These trends are readily understood. At high redshifts, galaxies are less-massive and therefore fainter. Thus it is extremely unlikely to be as bright as 25 mag. The opposite is true for the faintest limiting magnitude ($m_{lim} = 31$), which shows an increase in the fraction with redshift. Due to the steep mass function, the abundances of faint galaxies, at $z = 2$, is large and the fraction that are MW progenitors is consequently low; by redshift $z = 8$ those low-mass galaxies have dropped below this limiting magnitude and the MW progenitors become more prominent.

The fractions of galaxies in each bin shown in the left-hand panel of Fig. 7 vary considerably with redshift. In the right-hand panel of Fig. 7, we use a fixed magnitude range around the median of MW-like progenitors (shown in the left-hand panel of Fig. 5). These ranges correspond to ± 0.5 dex around the median magnitude for MW-like progenitors at each redshift, shown in purple. The magnitude range in this panel has its highest fraction (~ 11 per cent) at redshift $z = 2$ and its lowest (~ 1 per cent) at redshift $z = 6$. The fractions in this panel end at redshift $z = 6$ since beyond this time more than 50 per cent of the progenitors are unidentified (as in Fig. 5). At high redshifts ($z = 6$), it is clear that there are many galaxies with a similar magnitude as the MW-like progenitors that do not become MW-like galaxies by the present. The key difference between these galaxies and the progenitors of MW-like galaxies is simply that they either merge with their host galaxy (similar

to a GES type merger event) or become satellites (similar to the LMC).

4.1 MW progenitors with realistic accretion histories

In this section, we focus on the small sample of seven MW analogues with the additional constraints on the accretion history, namely having a GES-like merger and a LMC satellite. See Section 2 and Evans et al. (2020) for details. The dark matter and star particles around these MW analogues at $z = 2$ are shown in Figs 8 and 9, respectively. The main progenitor of the MW-like object is positioned at the centre of each image and is marked with a white circle. LMC and GES progenitors are also marked with orange and red circles, respectively. Each panel has a side length of ~ 1.13 Mpc, which corresponds to the size of the FoV of JWST/NIRCam (2.2×2.2 arcmin) at redshift $z = 2$.⁶ These two figures were made using PY-SPHVIEWER (Benitez-Llambay 2015), with 64 of the nearest neighbours used for calculating the SPH smoothing length.

GES progenitors are close to the MW progenitors at this redshift. This is expected as they are constrained to merge with the main progenitor at $z = 1 - 2$. Interestingly, all of LMC progenitors are well within the JWST/NIRCam FoV size. We will elaborate on the distance of LMC and GES progenitors at various redshifts below.

The cyan squares in Figs 8 and 9 mark the regions of these systems that have been illustrated in the mock JWST images shown in Fig. 10. These have been produced using a background mock image for JWST/NIRCam of the GOODS-S field (from Williams et al. 2018) on to which the images of our MW-analogues have been overlaid. Due to the small, faint nature of our simulated galaxies, they have been assigned a pink colour for easy identification in the image. *These colours are not illustrative of real life observations.* This figure shows that without redshift information and potentially other constraints, identifying the progenitors of the MW and its

⁶Note these are not light cones, rather particles at a fixed redshift (fixed snapshot) of the simulation.

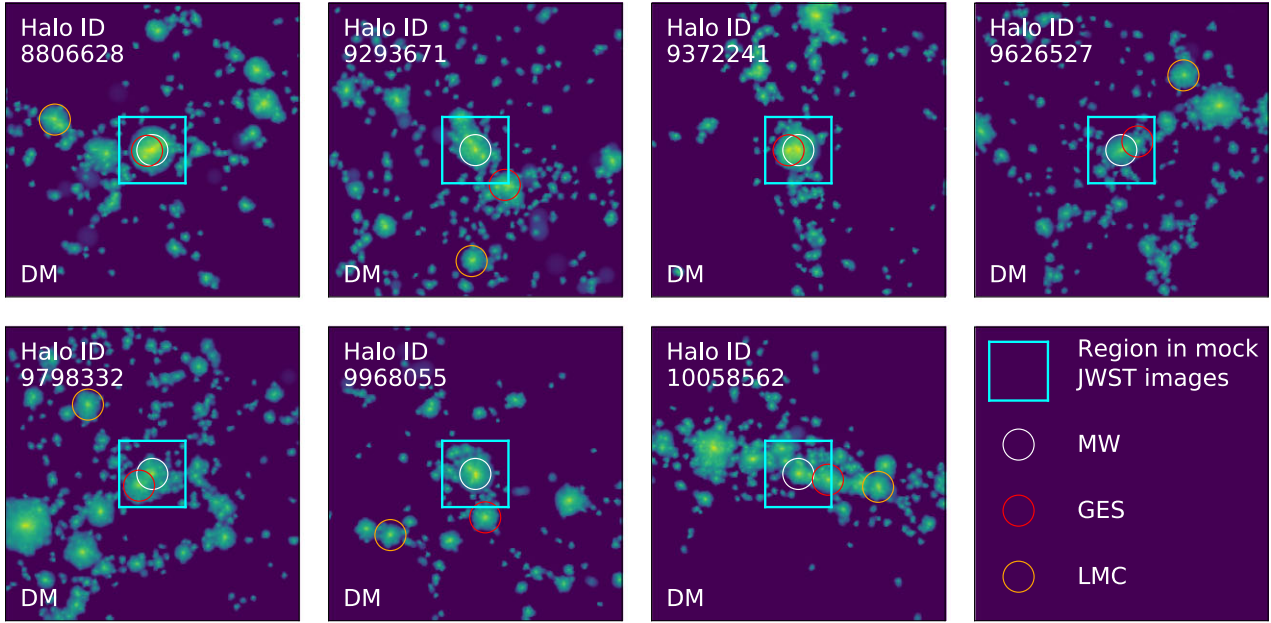


Figure 8. Dark matter distribution around seven MW analogues with a GES and LMC (see text for details), shown at redshift $z = 2$. Each panel shows a random projection of particles within a radius of 0.8 Mpc centred on the main progenitor of the MW analogue, which is marked with a white circle. Red and orange circles represent the positions of the centre of the GES and LMC progenitors, respectively. Image panels have a side length of ~ 1.13 Mpc and the size of the *JWST*/NIRCam FoV (2.2×2.2 arcmin) at $z = 2$. The cyan square in each panel indicates the region size for the mock images in Fig. 10. Smoothed particle images were made using PY-SPHVIEWER (Benitez-Llambay 2015).

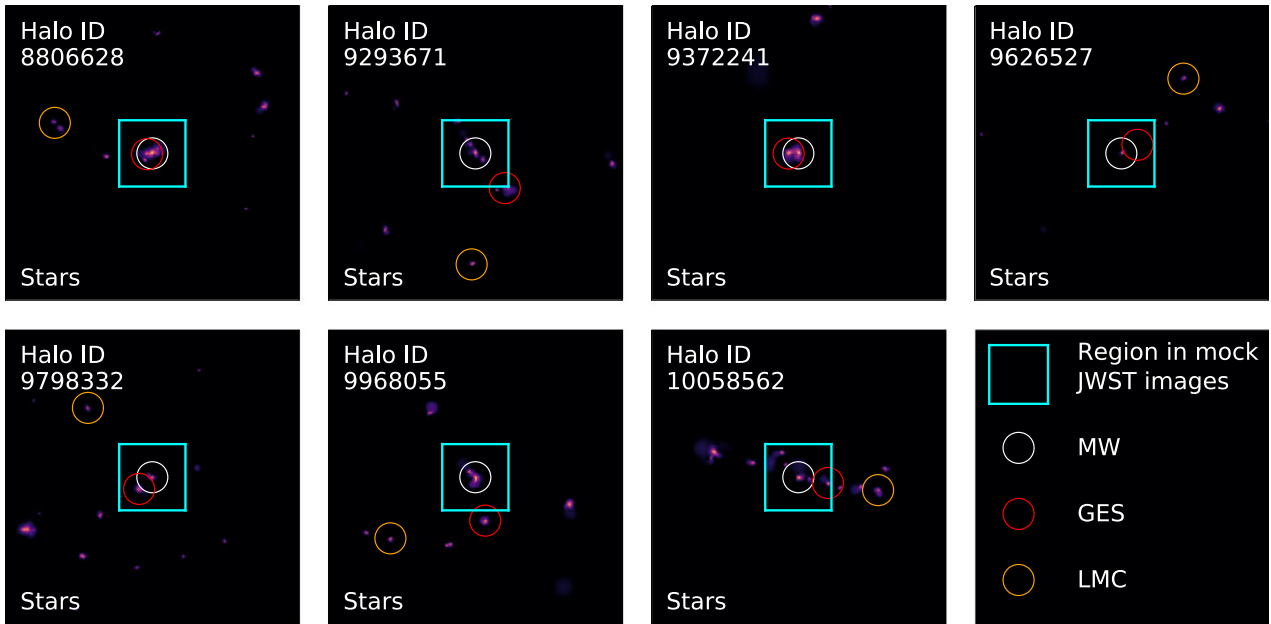


Figure 9. Same as Fig. 8 but for star particles in the same region.

building blocks amongst all the foreground and background galaxies will be very difficult.

To further investigate the proximity of the LMC and GES progenitors to the MW progenitor at various redshift, their angular and physical separations are shown in Fig. 11. The left-hand panel shows the median and [16th–84th] percentile of the angular separation between progenitors of the MW- and LMC-like galaxies, as well as of the MW- and GES-like ones. Angular separations are based on the average of three orthogonal projections. We additionally

include individual lines for the subsample of 7 MW analogues (and the corresponding LMC and GES) where we show the maximum separation (i.e. 3D distance).

The left-hand panel in Fig. 11 shows that both the LMC and GES progenitors fall within the *JWST*/NIRCam FoV (120 arcsec) at all times, with GES progenitors being invariably closer to the MW than the LMC progenitors. Individual galaxies are shown as fine dashed lines for the seven MW analogues. Note that one of the LMC satellites is much further away so is not visible in the ‘Halo ID

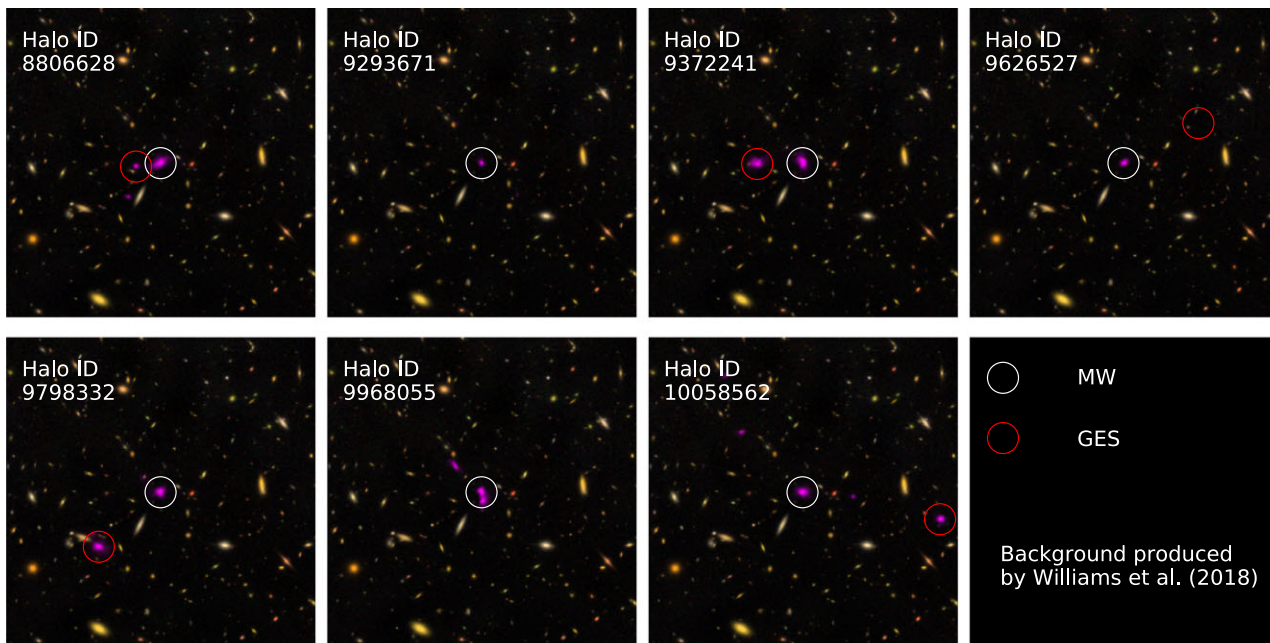


Figure 10. Mock *JWST* images of MW analogue systems, each panel shows a 30×30 arcsec² FoV. Stars in the MW analogue systems are shown in pink to emphasize their particle locations; this is not a representative of their observed colour. The background of these images were produced by Williams et al. (2018) to illustrate the *JWST* view of the GOODS-S field. The MW and GES galaxies are highlighted using white and red circles, respectively.

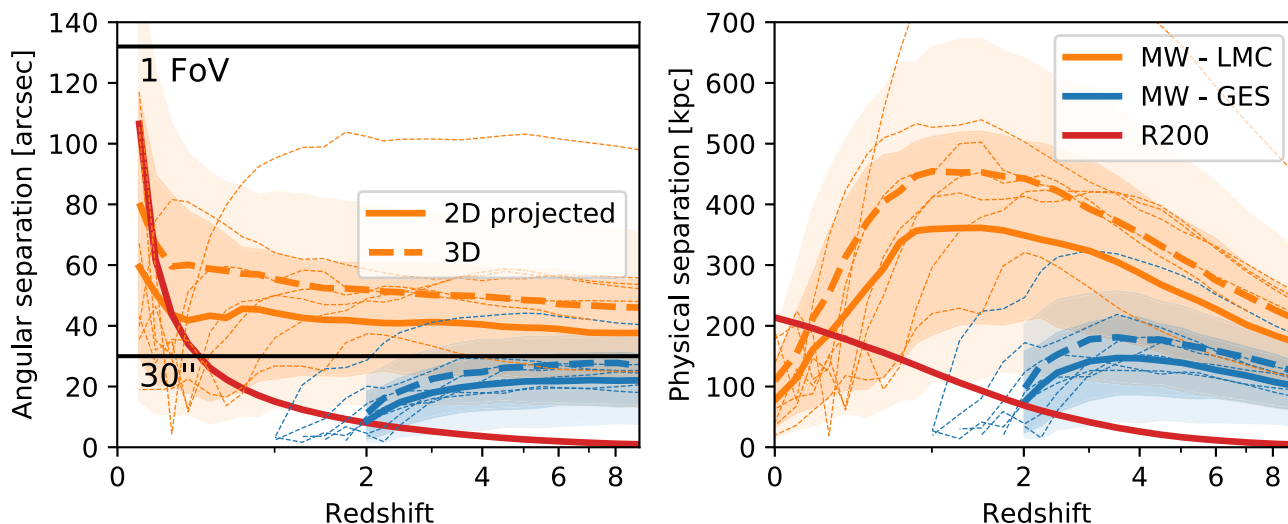


Figure 11. *Left*: angular separation of LMC-like (orange) and GES-like galaxies (blue) from their host, i.e. the progenitors of MW-like galaxies, as a function of redshift. The thick solid lines and the shaded regions of corresponding colour represent the median, [16th–84th] and [5th–95th] percentile ranges of projected separations for the LMC-like and GES-like groups, whereas the thick dashed lines show the median 3D separations for these groups. Thin dashed lines correspond to 3D separations for the MW analogues group (and their LMC- and GES-like accretions). Since GES is defined as merging between redshifts $z = 1 - 2$, the separations are only shown until redshift $z = 2$. Both the LMC- and GES-like galaxies fit within the same *JWST* FoV as their host, i.e. separation < 2.2 arcmin. *Right*: similar to the left-hand panel but for (proper) physical separation. The red lines in both panels show the median R_{200} of MW-like galaxies as a function of redshift. The projected separations are based on the average along three orthogonal axes.

9372241” panel in Fig. 8. The separations between MW- and GES-like progenitor galaxies end at redshifts $z = 2$ since this is where some GES galaxies start to merge with their host galaxies and the median is no longer representative of the whole sample. The angular resolution limit of *JWST*/NIRCam of 0.07 arcsec (at 2 microns) indicates that all GES progenitors can be resolved from their MW progenitor companion.

The right-hand panel of Fig. 11 is similar to the left-hand panel but shows the physical separation. The turnaround time and infall

time of the objects are easier to see here. The R_{200} evolution of a MW analogue is shown with a red curve in both panels for reference. LMC-like satellites have a recent infall time, $z \sim 0.3$, consistent with previous works (e.g. Boylan-Kolchin, Besla & Hernquist 2011a; Rocha, Peter & Bullock 2012). Such massive satellites are affected by dynamical friction to a large degree and they merge quickly with the host; hence, those surviving at redshift at $z = 0$ must have fallen recently (e.g. Fattahi et al. 2020). The turnaround redshift and radius of the LMC sample are on average $z \sim 1.5$ and $r = 360 \pm 160$

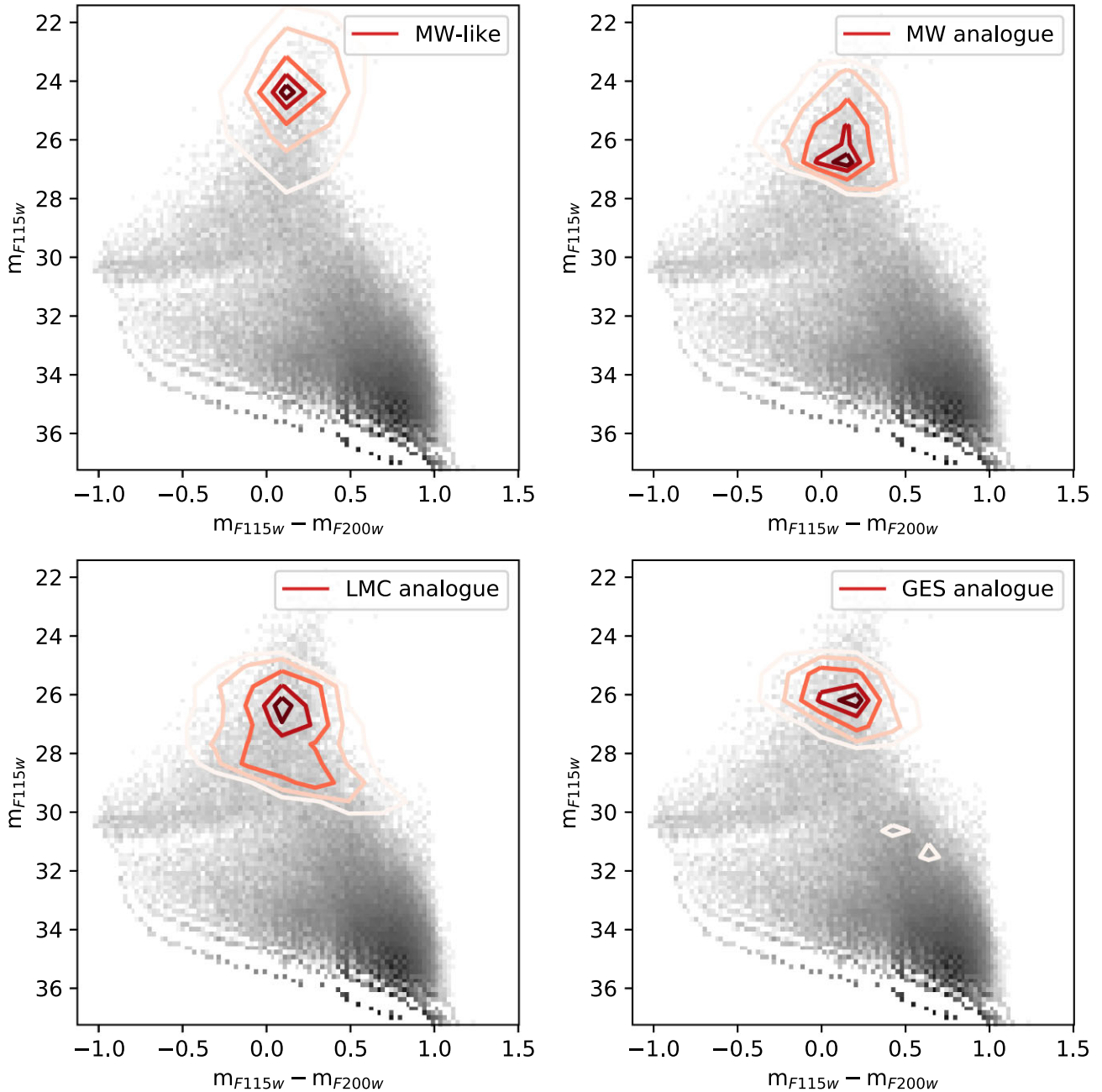


Figure 12. The CMDs for galaxies in the F115W and F200W passbands at redshift $z = 2$. The greyscale background shows the colour-magnitude distribution for all galaxies in EAGLE-Recal; the red contours represent the area of the CMD that 10 per cent, 25 per cent, 50 per cent, 75 per cent, and 90 per cent of the progenitors of MW-like, MW analogues, and their LMC and GES components would be contained in the upper-left to lower-right panels, respectively. The mass distribution of MW-like galaxies is quite broad, which causes a large spread in magnitudes.

kpc, respectively. GES analogues have a smaller turnaround radius ($r = 150 \pm 60$ kpc) and earlier accretion times ($z \sim 3.5$), compared to LMC progenitors. This is expected since GES are constrained to merge with the MW progenitors by $z = 1$.

Combining the results from Fig. 5 and Table 3, we conclude that MW-like progenitor galaxies should be observable up until $z \sim 6$ in most *JWST*/NIRCam passbands, with associated LMC- and GES-like galaxies observable until redshifts $z \gtrsim 4$ and 5.3, respectively. At these times, the LMC- and GES-like galaxies will most likely be within the *JWST*/NIRCam FoV.

4.1.1 Colour-magnitude diagrams

We now consider whether or not progenitors of the MW, LMC, and GES are distinguishable from other galaxies at the same redshift. We turn to the colour-magnitude diagrams (CMDs) for another layer of information. Fig. 12 shows the CMD for the progenitor in the F115W versus F115W-F200W plane at $z = 2$. These passbands were chosen at random since at $z = 2$ there were minimal differences between CMDs.

We show all MW-like galaxies and the individual components of the seven MW analogues (MW, LMC, and GES) in various

panels in Fig. 12 from top-left to lower-right, respectively. The background shows a greyscale density distribution for the overall colour-magnitude distribution of the total population of galaxies in the EAGLE-Recal run that has higher resolution. At fainter magnitudes, we see individual ‘ridges’ that are likely caused by resolution effects. Similarly to the approach used for Fig. 5, we do not use the magnitudes (and colours) directly from the EAGLE-Ref run for our target galaxies, especially because the LMC and GES progenitors at high redshifts have relatively low-stellar mass. Instead, we highlight with red contours the location where galaxies with similar stellar masses to our target galaxies lie on the CMD.

The top-left panel of Fig. 12 shows that the progenitors of MW-like galaxies are among the brightest galaxies at $z = 2$ with magnitudes brighter than $m_{F115W} \sim 26$. However, MW analogues (top-right panel) lie at the lower magnitude ranges for all MW-like galaxies. This is consistent with the stellar mass evolution shown in Evans et al. (2020) where MW analogues have a much lower mass than typical MW-like galaxies. The MW, LMC, and GES analogues all lie within a similar space in the CMD, with a greater range in colour space than magnitude space. They tend to have magnitudes around 26 and colour between -0.5 and 0.5 , in these passbands.

We include a similar figure but for CMDs at redshift $z = 4, 6$, and 8 in Appendix B. In summary, the results discussed above hold at those redshifts too. We note that at $z = 6$ and 8 , some combination of colours in *JWST*/NIRCam passbands will not yield useful CMDs, as some passbands are in the Lyman-break, as shown in Appendix C. More precisely, F070W at $z = 6$ is bluer than the Lyman-break, and both F070W and F090W are bluer by $z = 8$.

5 DISCUSSION AND CONCLUSIONS

We provide predictions for *JWST* using cosmological hydrodynamical simulations from the EAGLE project Schaye et al. (2015). We have calculated dust-free magnitudes in *JWST*/NIRCam bands for all galaxies, and then applied a simple-analytic dust correction using the ISM column density and temperature along the line of sight (based a modified version of Dust Model B from Vogelsberger et al. 2020). The dust-corrected magnitudes were used to produce comoving galaxy luminosity functions at redshifts $z = 2$ – 8 , along with the estimated number of galaxies in a *JWST*/NIRCam FoV across the same redshift range. In the second half of this paper, we focused on MW analogues and the main accreted objects on to them, namely LMC- and GES-like objects, as identified in Evans et al. (2020), to see how far back in time their progenitors might be observable, and if it might be possible to identify them in a *JWST*/NIRCam FoV. Our main conclusions are as follows:

(i) We compare our results with those from Vogelsberger et al. (2020) which is based on Illustris-TNG, and a more sophisticated treatment of dust attenuation using radiative transfer code, SKIRT. We find excellent agreement between the two results when comparing M_* versus dust-corrected magnitudes (M_{UV}).

(ii) Our luminosity functions are in overall agreement with those from Vogelsberger et al. (2020). Considering the previous point, the differences in the luminosity functions are likely caused by differences in the stellar mass functions of EAGLE and Illustris-TNG, resulting from their different subgrid galaxy formation models. Our luminosity functions are also in good agreement with those produced from the JAGUAR mock catalogue for *JWST* (Williams et al. 2018), however, the JAGUAR luminosity functions are flatter

at the bright end and hence our results may underestimate the number of bright galaxies observable with *JWST*/NIRCam.

(iii) The best-fitting parameters for the Schechter functions were used to predict the expected number counts of galaxies at each redshift. We expect a maximum of ~ 2400 galaxies at redshift $z = 2$ and ~ 80 at redshift $z = 8$ for an exposure time of 10^5 s ($SNR = 5$). These numbers reduce to ~ 1300 and ~ 8 at those two redshifts, respectively, for exposure time of 10^4 s ($SNR = 10$). These predictions are overall lower than the average numbers from Vogelsberger et al. (2020). This discrepancy does not affect the MW progenitor results because MW progenitor galaxies are among the fainter galaxy population. It would, however, affect the numbers predicted in an FoV, especially at redshift 8 since at this redshift, the counts are no longer dominated by the faint end for the 10^4 s exposure. We found that our predicted numbers of galaxies are consistent with Cowley et al. (2018), who used the semi-analytic model of galaxy formation, Galform.

(iv) Assuming an exposure time of 10^5 s and $SNR = 5$, a MW-like progenitor galaxy would be observable with *JWST* up to redshift $z \sim 6$, whereas progenitors of LMC- and GES-like galaxies would be observable out to redshifts $z \sim 4$ and 5.3 , respectively. The optimal passband is F356W and the least sensitive is F070W. In the F356W passband, *JWST* should be able to observe galaxies on average out to $\Delta z = 1$ more than in the F070W passband. These limits reflect the fact the these passbands have the best and worst transparency respectively.

(v) The progenitors of the individual components of the MW analogue systems (MW, LMC, and GES galaxies) have very similar stellar masses and magnitudes at high redshifts, with GES analogues being on average slightly more massive than the LMC analogues. The main difference in their fate lies in whether they become a host galaxy, satellite galaxy, or if they merge with their host galaxy.

(vi) The median magnitudes of progenitors of LMC-like galaxies at $z = 2$ is consistent with predictions made by Boylan-Kolchin et al. (2015) who estimate that the LMC would have had a dust-free absolute UV magnitude of -15.6 ± 0.8 . Our dust-free absolute M_{UV} for LMC-like galaxies at $z = 2$ is $M_{UV} \sim -15.7$.

(vii) Our results suggest that the progenitors of the LMC- and GES-like galaxies always lie within 60 and 30 arcsec, respectively, of MW progenitors at all times and therefore will fit within one FoV of *JWST*/NIRCam.

(viii) The CMDs of the progenitors of MW analogues also suggest that the three components (MW, LMC, and GES) should lie in a similar colour-magnitude range. Galaxies of similar mass to the MW-, LMC-, and GES-like galaxies in the MW analogue systems have a wide range of colours but a narrow range in magnitude.

In summary, our simulations indicate that it should be possible to observe progenitors of MW analogues using *JWST* and also observe the progenitors of their LMC-like satellites and GES-like companions at early times. Up until the redshift at which they are observable (typically $z = 4$), the three galaxies should all fall within the same FoV. At redshift $z = 2$, galaxies with similar mass and $m_{F115W} \sim 26$ could be analogues to the MW/GES merger. This is an exciting opportunity to link the high redshift universe to our galaxy today.

In closing, we remark that our study can be extended and refined with future generations of simulations, which will provide larger volumes and/or finer resolution. The EAGLE-Ref simulations span 100 Mpc^3 but, there are only 7 MW-analogues in this volume. Larger simulations will allow for better statistics and hence firmer

conclusions can be made for MW analogue galaxies. With better statistics, we could also investigate MW-like systems within the Local Group environment (and hence provide comparisons with work such as Boylan-Kolchin et al. 2016; Santistevan et al. 2020). Finally, higher resolution simulations would allow us to calculate the surface brightness and size of low-mass galaxies (which would allow for comparisons with work such as Patej & Loeb 2015).

ACKNOWLEDGEMENTS

We thank Calvin Sykes for sharing the ENGINe data with us, we also thank Mathilde Jauzac and Renkse Smit for their helpful comments on this manuscript. AD thanks the staff at the Durham University Day Nursery who play a key role in enabling research like this to happen. TE is supported by a Royal Society Research Grant. AD is supported by a Royal Society University Research Fellowship. AD acknowledges support from the Leverhulme Trust and the Science and Technology Facilities Council (STFC) [grant numbers ST/P000541/1, ST/T000244/1]. AF is supported by the UK Research and Innovation (UKRI) Future Leaders Fellowships (grant numbers MR/V023381/1, MR/T042362/1). CSF acknowledges European Research Council (ERC) Advanced Investigator grant DMIDAS (GA 786910). This work used the DiRAC@Durham facility managed by the Institute for Computational Cosmology on behalf of the STFC DiRAC HPC Facility (www.dirac.ac.uk). The equipment was funded by BEIS capital funding via STFC capital grants ST/K00042X/1, ST/P002293/1, ST/R002371/1 and ST/S002502/1, Durham University and STFC operations grant ST/R000832/1. DiRAC is part of the National e-Infrastructure.

DATA AVAILABILITY

The data used in this article are available in the EAGLE online data base, at <http://virgodb.dur.ac.uk:8080/Eagle>.

REFERENCES

- Amorisco N. C., 2017, *MNRAS*, 464, 2882
 Asplund M., Grevesse N., Sauval A. J., Scott P., 2009, *ARA&A*, 47, 481
 Baes M., Verstappen J., Looze I. D., Fritz J., Saftly W., Pérez E. V., Stalevski M., Valcke S., 2011, *ApJS*, 196, 22
 Beichman C. A., Rieke M., Eisenstein D., Greene T. P., Krist J., McCarthy D., Meyer M., Stansberry J., 2012, Conference proceedings: Space Telescopes and Instrumentation 2012, 8442, 84422N
 Belokurov V., Erkal D., Evans N. W., Koposov S. E., Deason A. J., 2018, *MNRAS*, 478, 611
 Benitez-Llambay A., 2015, py-sphviewer: Py-SPHViewer v1.0.0. <https://zenodo.org/record/21703>, Last accessed 25/11/21
 Benson A. J., Frenk C. S., Lacey C. G., Baugh C. M., Cole S., 2002, *MNRAS*, 333, 177
 Bouwens R. J. et al., 2015, *ApJ*, 803, 34
 Bouwens R. J. et al., 2016, *ApJ*, 830, 67
 Bouwens R. J. et al., 2021, *AJ*, 162, 47
 Boylan-Kolchin M., Besla G., Hernquist L., 2011a, *MNRAS*, 414, 1560
 Boylan-Kolchin M., Bullock J. S., Kaplinghat M., 2011b, *MNRAS*, 415, L40
 Boylan-Kolchin M., Weisz D. R., Johnson B. D., Bullock J. S., Conroy C., Fitts A., 2015, *MNRAS*, 453, 1503
 Boylan-Kolchin M., Weisz D. R., Bullock J. S., Cooper M. C., 2016, *MNRAS*, 462, L51
 Busha M. T., Marshall P. J., Wechsler R. H., Klypin A., Primack J., 2011, *ApJ*, 743, 40
 Callingham T. M. et al., 2019, *MNRAS*, 484, 5453
 Calvi V. et al., 2016, *ApJ*, 817, 120
 Calzetti D., Armus L., Bohlin R. C., Kinney A. L., Koornneef J., Storchi-Bergmann T., 2000, *ApJ*, 533, 682
 Camps P., Baes M., 2015, *Astron. Comput.*, 9, 20
 Camps P., Baes M., Saftly W., 2013, *A&A*, 560, A35
 Chabrier G., 2003, *PASP*, 115, 763
 Charlot S., Fall S. M., 2000, *ApJ*, 539, 718
 Choi J., Dotter A., Conroy C., Cantiello M., Paxton B., Johnson B. D., 2016, *ApJ*, 823, 102
 Conroy C., Gunn J. E., 2010, *ApJ*, 712, 833
 Conroy C., Gunn J. E., White M., 2009, *ApJ*, 699, 486
 Cowley W. I., Baugh C. M., Cole S., Frenk C. S., Lacey C. G., 2018, *MNRAS*, 474, 2352
 Crain R. A. et al., 2015, *MNRAS*, 450, 1937
 Davis M., Efstathiou G., Frenk C. S., White S. D. M., 1985, *ApJ*, 292, 371
 Dotter A., 2016, *ApJS*, 222, 8
 Elias L. M., Sales L. V., Helmi A., Hernquist L., 2020, *MNRAS*, 495, 29
 Erkal D. et al., 2019, *MNRAS*, 487, 2685
 Evans N. W., 2020, *Proceedings of the International Astronomical Union*, 14, 113
 Evans T. A., Fattahi A., Deason A. J., Frenk C. S., 2020, *MNRAS*, 497, 4311
 Fattahi A. et al., 2019, *MNRAS*, 484, 4471
 Fattahi A. et al., 2020, *MNRAS*, 497, 4459
 Finkelstein S. L. et al., 2015, *ApJ*, 810, 71
 Forbes D. A., 2020, *MNRAS*, 493, 847
 Gaia Collaboration, 2018, *A&A*, 616, A1
 Helmi A., Babusiaux C., Koppelman H. H., Massari D., Veljanoski J., Brown A. G. A., 2018, *Nature*, 563, 85
 Horta D. et al., 2021, *MNRAS*, 500, 1385
 Kriek M., Conroy C., 2013, *ApJ*, 775, L16
 Kruijssen J. M. D. et al., 2020, *MNRAS*, 498, 2472
 Liu L., Gerke B. F., Wechsler R. H., Behroozi P. S., Busha M. T., 2011, *ApJ*, 733, 62
 Mackereth J. T. et al., 2019, *MNRAS*, 482, 3426
 Naidu R. P., Conroy C., Bonaca A., Johnson B. D., Ting Y.-S., Caldwell N., Zaritsky D., Cargile P. A., 2020, *ApJ*, 901, 48
 Naidu R. P. et al., 2021, *ApJ*, 923, 92
 Noll S., Burgarella D., Giovannoli E., Buat V., Marcillac D., Munoz-Mateos J. C., 2009, *A&A*, 507, 1793
 Oesch P. A. et al., 2013, *ApJ*, 773, 75
 Oesch P. A. et al., 2014, *ApJ*, 786, 108
 Oesch P. A., Bouwens R. J., Illingworth G. D., Labbé I., Stefanon M., 2018, *ApJ*, 855, 105
 Patej A., Loeb A., 2015, *ApJ*, 815, L28
 Patel E., Besla G., Sohn S. T., 2017a, *MNRAS*, 464, 3825
 Patel E., Besla G., Mandel K., 2017b, *MNRAS*, 468, 3428
 Paxton B., Bildsten L., Dotter A., Herwig F., Lesaffre P., Timmes F., 2011, *ApJS*, 192, 3
 Paxton B. et al., 2013, *ApJS*, 208, 4
 Paxton B. et al., 2015, *ApJS*, 220, 15
 Penarrubia J., Gomez F. A., Besla G., Erkal D., Ma Y.-Z., 2016, *MNRAS*, 456, L54
 Planck Collaboration, 2014, *A&A*, 571, A1
 Rocha M., Peter A. H. G., Bullock J., 2012, *MNRAS*, 425, 231
 Saftly W., Baes M., Camps P., 2014, *A&A*, 561, A77
 Sanchez-Blazquez P. et al., 2006, *MNRAS*, 371, 703
 Santistevan I. B., Wetzel A., El-Badry K., Bland-Hawthorn J., Boylan-Kolchin M., Bailin J., Faucher-Giguère C.-A., Benincasa S., 2020, *MNRAS*, 497, 747
 Sawala T. et al., 2016, *MNRAS*, 457, 1931
 Schaller M. et al., 2015, *MNRAS*, 451, 1247
 Schaye J. et al., 2015, *MNRAS*, 446, 521
 Schechter P., 1976, *ApJ*, 203, 297
 Seaton M. J., 1979, *MNRAS*, 187, 73P
 Song M. et al., 2016, *ApJ*, 825, 5
 Springel V., 2005, *MNRAS*, 364, 1105
 Stefanon M. et al., 2017, *ApJ*, 851, 43

- Tacchella S., Bose S., Conroy C., Eisenstein D. J., Johnson B. D., 2018, *ApJ*, 868, 92
- Thob A. C. R. et al., 2019, *MNRAS*, 485, 972
- Tollerud E. J., Barton E. J., Bullock J. S., Trinh C., 2011, *EAS Publ. Ser.*, 48, 455
- Tomczak A. R. et al., 2014, *ApJ*, 783, 85
- Trayford J. W. et al., 2015, *MNRAS*, 452, 2879
- Vogelsberger M. et al., 2020, *MNRAS*, 492, 5167
- Williams C. C. et al., 2018, *ApJS*, 236, 33
- Yung L. Y. A., Somerville R. S., Finkelstein S. L., Popping G., Dave R., 2019, *MNRAS*, 483, 2983

APPENDIX A: RESOLUTION CHECKS AND MAGNITUDE CORRECTIONS

We compare the dust-corrected apparent magnitudes for all galaxies in the EAGLE-Ref and EAGLE-Recal volumes in order to quantify the effects of resolution on our results. The relationship between apparent magnitude and stellar mass for the two volumes is shown in Fig. A1. The median values for the two volumes are consistent with each other. However, as shown in the figure, there is a large amount of scatter at the low-mass end for the EAGLE-Ref volume due to the lack of resolution.

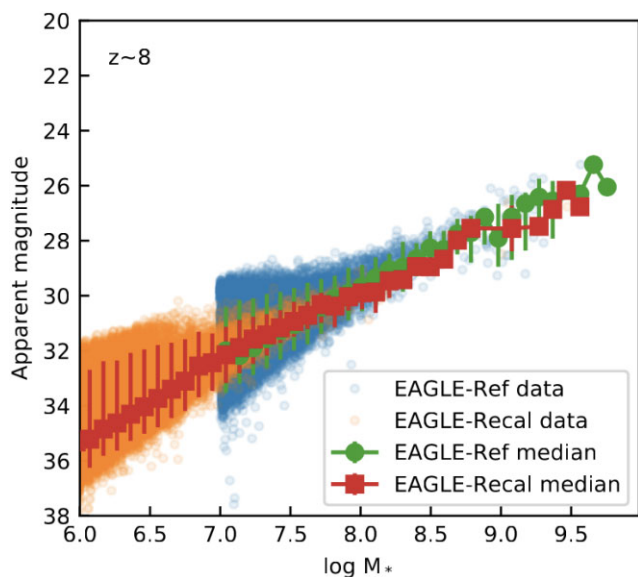


Figure A1. The relationship between apparent magnitude and stellar mass for the EAGLE-Ref (blue points) and EAGLE-Recal (orange) volumes at $z = 8$. The median values for each sample are shown as green circles and red squares for EAGLE-Ref and EAGLE-Recal, respectively. The errorbars represent the [5th–95th] percentiles of the data.

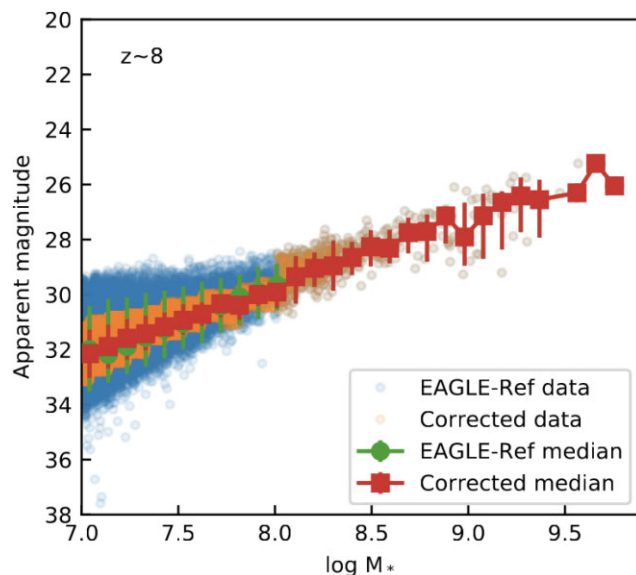


Figure A2. The apparent magnitude–stellar mass relation for the uncorrected (blue points) and corrected (orange points) EAGLE-Ref data.

In order to get a better representation of the magnitudes at the low-mass end, we apply a magnitude correction to galaxies of stellar mass $M_* < 10^8 M_\odot$ as this is where the scatter in the EAGLE-Ref data starts to increase dramatically. Such corrections, however, are not necessary for brighter galaxies as these are resolved with enough star particles. (See agreement at the bright end in Fig. A1).

For the magnitude corrections below $M_* < 10^8 M_\odot$, we model the distribution of apparent magnitudes for the higher resolution Recal50 data set in a given mass bin between the [5th–95th] percentile values (shown as red errorbars on Fig. A1) and resample values for EAGLE-Ref from this distribution. These corrections are performed at all redshifts for magnitudes with and without dust, and for all passbands used in this work.

Fig. A2 shows the original data from EAGLE-Ref (blue points) and the new corrected magnitudes (orange points). As shown in the figure, the median values are unchanged. The corrected magnitude data points no longer show such a large scatter at the low-mass end.

APPENDIX B: CMDS AT HIGH REDSHIFT

Fig. B1 shows the CMDs for the m_{F115W} and m_{F200W} passbands at high redshifts. The red contours in each redshift panel highlight the regions where progenitors of MW-like galaxies are most likely to reside. As the redshift increases, the MW-like progenitors occupy a larger region of the CMD; by redshift $z = 8$, the contours cover the entirety of the CMD, but are more concentrated at fainter magnitudes and redder colours.

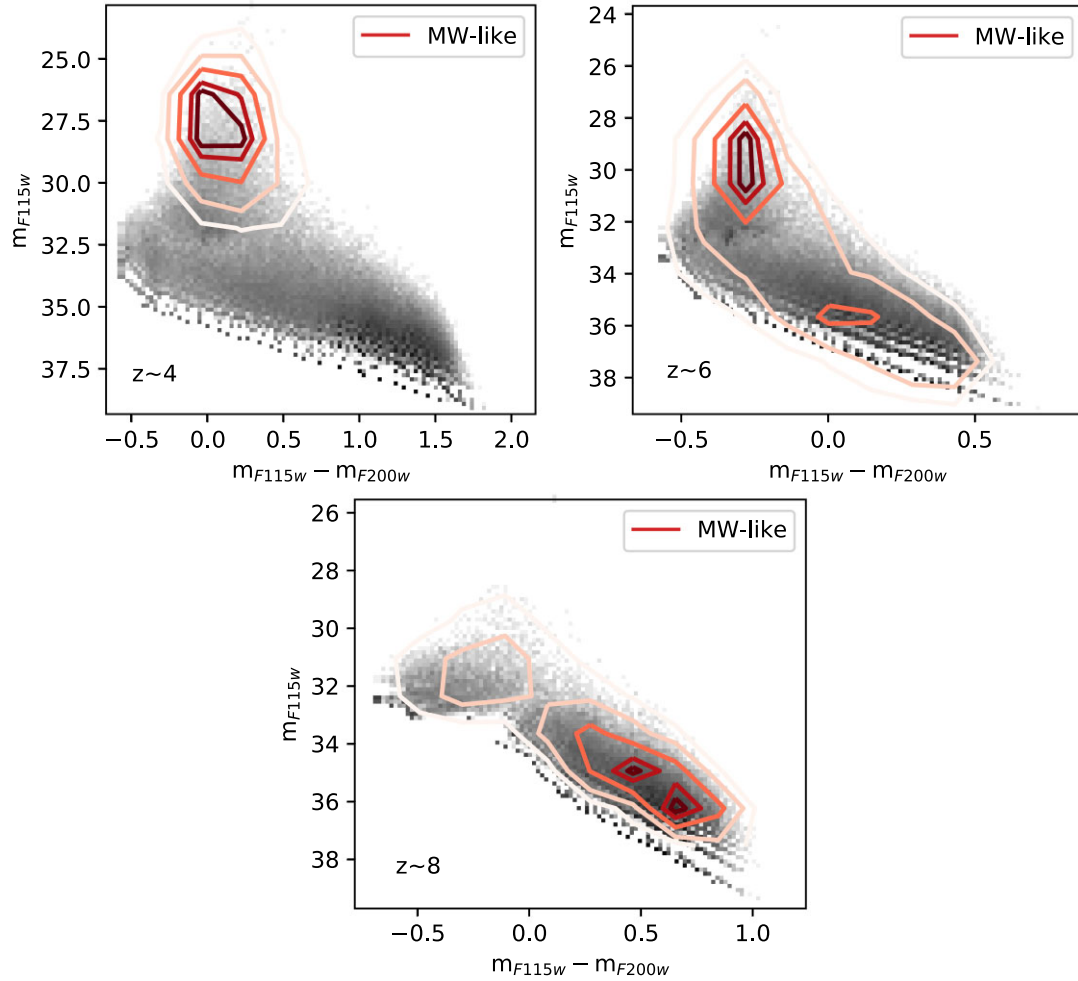


Figure B1. CMDs for all EAGLE-Recal galaxies (grey) at redshifts $z = 4, 6,$ and 8 with overlaid red contours to show the region where 10, 25, 50, 75, and 90 per cent of MW-like galaxies are enclosed.

APPENDIX C: MILKY WAY ANALOGUES AS LYMAN BREAK GALAXIES

The dust-free spectra of three MW-analogues are shown in Fig. C1. These spectra were made using the MILES Stellar library as part of FSPS, which include features such as absorption from the intergalactic medium and emission from nebulae.

The higher redshift spectra for the progenitors of these galaxies are shown as red and purple lines for $z = 6$ and 8 , respectively. These indicate that at these high redshifts, the progenitors of MW analogues could be seen as Lyman break galaxies in the bluer wavelength passbands, i.e. F070w, F090w, and F115W. The Lyman break features of these spectra may help distinguish MW-analogues from other galaxies in the field.

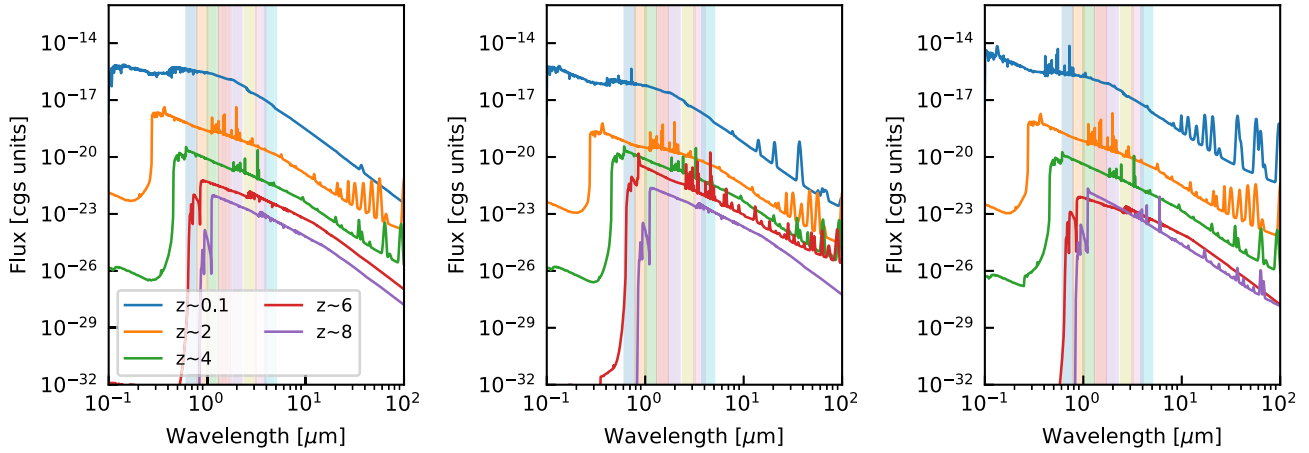


Figure C1. The dust free spectra of the progenitors of three of the MW analogues. Spectra are shown for each galaxy at redshifts $z = 0.1, 2, 4, 6,$ and 8 in blue, orange, green, red, and purple, respectively. The vertical coloured bands represent the *JWST*/NIRCam passbands (from left to right: F070W, F090W, F115W, F150W, F200W, F277W, F356W, and F444W). MW analogues may have Lyman break features at high redshifts, i.e. $z = 6$ and 8 .

This paper has been typeset from a $\text{\TeX}/\text{\LaTeX}$ file prepared by the author.